

NORTHWESTERN UNIVERSITY

Photonic Crystal Fiber Based Chemical Sensors for
Civil Structural Health Monitoring

A DISSERTATION

SUBMITTED TO THE GRADUATE SCHOOL
IN PARTIAL FULFILLMENT OF THE REQUIREMENTS

for the degree

DOCTOR OF PHILOSOPHY

Field of Civil and Environmental Engineering

By

SHIJIE ZHENG

EVANSTON, ILLINOIS

June 2013

UMI Number: 3563914

All rights reserved

INFORMATION TO ALL USERS

The quality of this reproduction is dependent upon the quality of the copy submitted.

In the unlikely event that the author did not send a complete manuscript and there are missing pages, these will be noted. Also, if material had to be removed, a note will indicate the deletion.



UMI 3563914

Published by ProQuest LLC (2013). Copyright in the Dissertation held by the Author.

Microform Edition © ProQuest LLC.

All rights reserved. This work is protected against unauthorized copying under Title 17, United States Code



ProQuest LLC.
789 East Eisenhower Parkway
P.O. Box 1346
Ann Arbor, MI 48106 - 1346

ABSTRACT

Photonic Crystal Fiber Based Chemical Sensors for
Civil Structural Health Monitoring

Shijie Zheng

A photonic crystal fiber (PCF) long-period grating (LPG) humidity sensor has been developed with high sensitivity and selectivity for nondestructive detection of moisture ingress into structures that can potentially lead to corrosion. We have proposed two types of nanofilms to be coated on the surface of air channels in the grating region of the fiber using electrostatic self-assembly deposition processing. The primary nanofilm does not affect LPG properties such as resonance wavelength or transmission intensity which can impact sensing characteristics; however it increases the sensitivity by changing the refractive index of the surrounding material. The secondary nanofilm is used for selectively adsorbing analyte molecules of interest. The experimental results reveal that, compared to the conventional fiber LPGs and exterior nanofilm-coated PCF-LPG, the interior nanofilm-coated PCF-LPG humidity sensors have higher resonance intensity change of $0.00022\%/10^{-3}\text{dBm}$ at relative humidity (RH) of 38% and average wavelength shift of $0.0007\%/pm$ in range of 22% to 29%. The proposed sensor shows excellent thermal stability as well.

Keywords: fiber-optic sensors, fiber Bragg grating gratings, long-period gratings, photonic crystal fiber, nanostructure material and film.

Acknowledgment

As I am approaching the end of my doctoral study at Northwestern University, I would like to thank the support from my committee members, Professor Sridhar Krishnaswamy, Professor Oluwaseyi Balogun, and Professor Jianmin Qu. As my academic advisor, Professor Krishnaswamy has been really supportive for my study and giving me helpful advice. Dr. Yinian Zhu has always been a good colleague and friend; I would like to thank his guidance as well. I also have received a lot of support and encouragement from my parents back in China, I want to say that I really love them, and want to thank them for their trust and support. You all made this happen!

Table of Contents

Abstract.....	2
Acknowledgment.....	3
List of Tables.....	6
List of Figures.....	7
Introduction.....;	15
Chapter 1--Numerical Calculation for PCF design.....	20
1.1 Simulation theories and tools.....	21
1.2 Parameter chosen and numerical analysis	22
1.3 Design results.....	24
Chapter 2--LPG principles and its fabrication on PCF.....	30
2.1 Modes in PCF for evanescent field sensing.....	30
2.2 Phase-matching condition and coupled-mode theory.....	32
2.3 LPG fabrication on PCF and characterization	33
2.4 Sensing mechanism.....	37
Chapter 3--Nano film coatings and its deposition on PCF	42
3.1 Nano films and its coating	42
3.2 ESA deposition process	43
3.3 Deposition on internal air channels of PCF---simulation and experiments.....	46
3.4 Nanofilms deposition and characterization.....	53
Chapter 4-- RH testing results and discussion.....	55

	5
4.1 RH response of SMF-28-LPG.....	55
4.2 RH response of nanofilm-coated SMF-28-LPG.....	58
4.3 Temperature responses of SMF-28-LPG and nanofilm-coated SMF-28-LPG.....	63
4.4 RH response of exterior nanofilm-coated PCF-LPG.....	65
4.5 RH response of interior nanofilm-coated PCF-LPG.....	67
Chapter 5--Tunable fiber ring laser absorption spectroscopic sensors for gas detection.....	72
5.1 Design of sensor head.....	75
5.2 Fabrication of sensor head.....	79
5.3 Tunable Er-doped fiber ring laser.....	83
5.4 Experiment set up.....	86
5.5 Testing results.....	88
5.6 Conclusion.....	90
References	91

List of Tables

Table 1: Optimized parameters and overlaps of IG-PCFs with air channels round and hexagonal latticed.....	25
Table 2: Average RH Sensitivity Comparison for Different Sensors.....	70
Table 3: Ammonia absorption lines.....	76
Table 4: Reflection parameters of normal fiber, PCF type-B, and PCF type-D with silver mirrors on the fiber facets.....	82

List of Figures

- Figure 1: Cross-sectional optical micrographs of endlessly single-mode IG-PCFs (fabricated by Yangtze Optical Fiber and Cable Company Ltd.) with (a) 5 rings of air-channel round latticed in cladding and (b) 5 rings of air-channel hexagonal latticed in cladding.....23
- Figure 2: Transverse Ex intensity distributions of symmetric cladding modes with maximum overlap with air channels round latticed for: (a) 4 rings of air-channel (fiber R-1), (b) 5 rings of air-channel (fiber R-2), and (c) 6 rings of air-channel (fiber R-3).....26
- Figure 3: Transverse Ex intensity distributions of symmetric cladding modes with maximum overlap with air channels hexagonally latticed for: (a) 4 rings of air-channel (fiber H-1), (b) 5 rings of air-channel (fiber H-2), and (c) 6 rings of air-channel (fiber H-3).....28
- Figure 4: Comparison of maximum overlap in air-channel with different parameters (d , Λ , and number of air-channel rings): (a) air channels in cladding are round arrayed and (b) air channels in cladding are hexagonally arrayed.....29

Figure 5: Linear polarization (LP) mode field intensity distributions in a PCF with 4 rings of air-channels hexagonally arranged, calculated at wavelength of 1550 nm for: (a) LP₀₁ fundamental core mode, (b) LP₀₂ cladding mode, (c) one state of degeneracy in LP₀₃ cladding mode, (d) LP₀₄ cladding mode, (e) LP₀₅ cladding mode, (f) LP₀₆ cladding mode, (g) one state of degeneracy in LP₀₇ cladding mode.....32

Figure 6: Schematic diagram of experimental setup for LPG inscribed in PCF by focused beam of CO₂ laser with a 1-D galvanometer (the insets are the cross-sectional optical micrograph of PCF and the outlook of PCF-LPG).....34

Figure 7: (a) Transmission spectra of the SMF-28-LPG with periods from 40 to 115 at interval of 5-period increase, (b) transmission spectra of the SMF-28-LPG before and after bonded to the RH testing frame as well as the simulated grating spectrum, and (c) transmission spectrum of PCF-LPG at resonance wavelength of 1597.10 nm with 69 periods.....36

Figure 8: Simulated power distributions of LP₀₄ cladding mode in PCF excited by a LPG (periodicity of 670 μm and period number of 14): (a) EX in amplitude, (b) EX in phase, (c) EY in amplitude, and (d) EY in phase birefringence of EX and EY, respectively.....39

Figure 9: Schematic diagram of core-to-cladding mode coupling in a PCF-LPG structure (the top-left inset is the cross-sectional optical micrograph of PCF, and the top-right inset illustrates that the mode coupling resonance strength depends strongly on the grating design with the number of grating periods being an important parameter).....40

Figure 10: Schematic illustration of ESA deposition processing with PAH⁺ or Al₂O₃⁺ (positive charge) water solution and PAA⁻ or PSS⁻ (negative charge) water solution for LPG nanostructure coatings.....44

Figure 11: SEM images of nanostructure coatings on optical fiber: (a) PAH⁺/PAA⁻ (10 bi-layers), (b) Al₂O₃⁺/PSS⁻ (10 bi-layers), and (c) PAH⁺/PAA⁻ (5 bi-layers) and Al₂O₃⁺/PSS⁻ (5 bi-layers).....45

Figure 12: Schematic diagram of capillary tube with liquid inside and contact angle: (a) the liquid is pushed out of the capillary by capillary force with contact angle large than 90° and (b) the liquid is pulled into the capillary by capillary force with contact angle smaller than 90°.....47

Figure 13: (a) Diagram of a cross-sectional PCF with 4 rings of air-channel in cladding (d: diameter of air-channel and Δd : distance of channel-to-channel separation), (b) numerically

calculated water filling time of air channels in different length of PCF-A with d of $3.76 \mu\text{m}$ and Δd of $8.99 \mu\text{m}$ at pressure differences of 2 bar, 3 bar, and 4 bar, and (c) numerically calculated water filling time of air channels in different length of PCF-B with d of $4.23 \mu\text{m}$ and Δd of $8.07 \mu\text{m}$ at pressure differences of 2 bar, 3 bar, and 4 bar.....48

Figure 14: (a) Schematic of compressed air pressure chamber for the filling of water/polymer solution, (b) picture showing a compressed air pressure chamber that can fill two PCFs simultaneously, and (c) picture showing a drop of water out of air channels of the PCF.....50

Figure 15: Dependence of pressurized water filling time on filling length with different pressure for (a) PCF (1) with air-channel diameter of $3.76 \mu\text{m}$, air-channel to air-channel distance of $7.03 \mu\text{m}$, and core diameter of $8.99 \mu\text{m}$ (the inset is the SEM image of PCF (1) cross-section) and (b) PCF (2) with air-channel diameter of $4.23 \mu\text{m}$, air-channel to air-channel distance of $8.07 \mu\text{m}$, and core diameter of $11.94 \mu\text{m}$ (the inset is the SEM image of PCF (2) cross-section).....52

Figure 16: SEM images for (a) cross-section of nanofilm-coated PCF with PAH⁺ and PAA⁻, (b) thickness of 3 bi-layers of PAH⁺ and PAA⁻, (c) cross-section of nanofilm-coated PCF with Al₂O₃⁺ and PSS⁻, and (d) thickness of 5 bi-layers of Al₂O₃⁺ and

PSS-.....52

Figure 17: Humidity chamber with the LPG fiber sensor fixed on a plastic frame, the moisture generator, and the humidity-meter.....56

Figure 18: (a) Transmission spectra of SMF-28-LPG for various RH from 20% to 50% and (b) dependence of SMF-28-LPG resonance wavelength and transmission intensity on RH.....57

Figure 19: (a) Experimental evolution of transmission spectra of SMF-28-LPG for: (a) the primary nanofilm before and after cleaned by Milli-Q water, in PAH^+ and PAA^- solutions, and after 10 bi-layers of $\text{PAH}^+/\text{PAA}^-$ coated and (b) the secondary nanofilm of the first bi-layer of $\text{Al}_2\text{O}_3^+/\text{PSS}^-$, in Al_2O_3^+ and PSS^- solutions, and after 10 bi-layer of $\text{Al}_2\text{O}_3^+/\text{PSS}^-$ coated.....60

Figure 20: (a) Transmission spectra of nanofilm-coated SMF-28-LPG for various RH from 19% to 25% and (b) dependence of nanofilm-coated SMF-28-LPG resonance wavelength and transmission intensity on RH.....62

Figure 21: Temperature responses of resonance wavelength and transmission intensity at RH of

20% for: (a) SMF-28-LPG and (b) nanofilm-coated SMF-28-LPG.....64

Figure 22: (a) Transmission spectra of exterior nanofilm-coated PCF-LPG for RH spans from 20% to 44% and (b) dependences of exterior nanofilm-coated PCF-LPG resonance wavelength and transmission intensity on different levels of RH.....66

Figure 23: Experimental setup for Relative Humidity test by interior nanofilm-coated PCF-LPG.....67

Figure 24: (a) Transmission spectra of interior nanofilm-coated PCF-LPG for RH spans from 22% to 29% and (b) dependences of interior nanofilm-coated PCF-LPG resonance wavelength and transmission intensity on different level of RH.....69

Figure 25: (a) Transmission spectra of interior nanofilm-coated PCF-LPG for RH spans from 21% to 40% and (b) dependences of interior nanofilm-coated PCF-LPG resonance transmission intensity on different level of RH by using a tunable Er-doped fiber ring laser as the light source.....71

Figure 26. Schematic diagram of core mode to cladding mode coupling and recoupling in a PCF-LPG with a silver mirror at the facet of the fiber.....77

Figure 27: Expected spectra of core mode and cladding mode coupling and recoupling in the sensor hard with a silver mirror at fiber facet: (a) tunable laser incident in PCF; (b) after LPG in PCF cladding; (c) after LPG in PCF core; (d) before reflection in PCF cladding; (e) before recoupling from PCF cladding at LPG; and (f) signal light out of PCF core.....78

Figure 28. SEM images of fiber facets coated with silver coatings: (a) normal fiber, (b) PCF type-B, (c) PCF type-D, and cleaved fiber cross-sections from 10 mm of silver coated fiber facets: (d) normal fiber, (e) PCF-type-B, (f) PCF type-D.....80

Figure 29: Optical spectra: (a) output of diode laser at wavelength around 1546 nm, (b) reflection intensity of normal fiber with silver mirror at fiber facet, (c) reflection intensity of PCF type-B with silver mirror at fiber facet, and (d) reflection intensity of PCF type-D with silver mirror at fiber facet.....81

Figure 30. Schematic diagram of tunable Er-doped fiber ring laser with the FFP-TF and the Sagnac loop. The insets show the tunable ring laser device box (left) and the interior components of the tunable ring laser (right).....84

Figure 31. (a) Optical output power spectrum of tunable Er-doped fiber ring laser, and (b) the

entire optical output power spectra of tunable laser with wavelength turning range from 1530.54 nm to 1559.64 nm.....85

Figure 32. Experimental setup for the absorption spectroscopic ammonia gas sensing.....87

Figure 33. (a) Optical spectrum of diode laser at wavelength of 1548.4 nm and (b) dependence of absorption laser intensity on ammonia concentration.....88

Figure 34. (a) Optical spectrum of tunable fiber ring laser at wavelength of 1563.6 nm and (b) dependence of absorption laser intensity on ammonia concentration.....89

Introduction

Corrosion affects our society on a daily basis, causing degradation and damage to civil structures including highway bridges, tunnels, power plants, buildings, and much more. One of the most critical reasons for such damage is the corrosion of reinforced concrete; NACE International (The Corrosion Society) estimates the cost of corrosion damage to concrete structures (in the USA) at approximately \$125 Billion per year [1]. And world-wide, the annual cost of \$ 2.2 trillion of corrosion related damage is over 3% of the world's GDP [2].

Corrosion typically happens in components reacting with its environment in which water plays an important role for initiating and sustaining electrochemical damage. The ingress of water acts as a transporting vehicle for aggressive agents, such as chloride and sulfate ions, to be penetrated into the concrete by capillary force. Water is also a reaction medium in destructive chemical processes, causing the corrosion of the concrete rebar. In general, the concentration of water in ambient air, which is expressed by relative humidity ($RH = P_m/P_{ms} \times 100\%$, where RH stands for relative humidity; P_m is the partial pressure of moisture; and P_{ms} is the pressure of moisture in saturation), has a significant effect on the corrosion mechanism. Therefore, it is important to develop a sensing tool such as a humidity sensor that can be easily integrated into the structure and which enables early detection of moisture ingress within reinforced concrete structures to remediate the situation before serious damage occurs.

Fiber optic sensors, with several advantages over traditional sensors such as light weight,

small size and strong immunity to electromagnetic interference, have been playing an important role in chemicals detection, including humidity (moisture). Fiber-optic grating refractometers have been increasingly explored for the interrogation of refractive index change of gas or aqueous solution [3], and long-period gratings (LPGs) as optical fiber humidity sensors have also been reported for applications in structural concrete condition monitoring to determine moisture ingress [4]. Other technology, such as light absorbance fiber optic sensor used in liquid PH or concentration detection, has been widely explored as well [5, 6]. In this work, we have developed an innovate sensing platform, a combination of Photonic Crystal Fiber (PCF) and Long Period Gratings(LPG) with enhanced evanescent field sensing providing a pathway to achieve high sensitivity and selectivity.

A photonic crystal fiber (PCF) consists of regularly spaced air channels running along the fiber cladding. Significant research work has been carried out recently towards the development of evanescent wave sensors using index-guiding photonic crystal fibers (IG-PCFs), also termed holey fibers or solid-core microstructured optical fiber [7-11]. The IG-PCFs are pure silica fibers with a two-dimensional fine array of air channels whose diameters range from sub-microns to tens of microns running axially along the fiber length [12, 13]. The IG-PCF retains the high-index core and low-index cladding contrast. It can trap and guide light in the core along the fiber via total internal refraction at a shallow enough angle of incidence but will refract light at steep angles on the core cladding boundary, as in conventional optical fibers. IG-PCFs possess many unique optical characteristics that can be tailored due to their intricate and versatile

air-silica cladding structure. Examples of IG-PCF applications include endlessly single mode [14] large mode area with high power transmission [15] high non-linearity [16] and broadly controllable dispersion [17]. As a new fiber-optic research frontier, IG-PCFs are being increasingly explored for a multitude of scientific and technological applications that range from novel optical and photonic devices to multi-modality sensors that take advantage of a light waveguide and a vapor/aqueous transmission cell [18, 19] permitting intensity-analyte interaction over long path length without the removal of fiber cladding. This is a very attractive feature for chemical detection without loss of mechanical integrity.

Long-period gratings (LPGs) [20], which are periodic index perturbation fabricated in a fiber with a periodicity typically ranging from 100 to 1000 μm and total grating length of several to tens of millimeters, provide an excellent means of coupling the forward-propagating linear polarization cladding modes (LP_{0m} , $m > 1$) under the phase-matching condition [21]:

$$\lambda_{r(m)} = [n_{co}^{eff}(n_{co}, n_{cl}, \lambda) - n_{cl-m}^{eff}(n_{cl}, n_{sur}, \lambda)] \Lambda_{LPG} \quad (1)$$

Where, $\lambda_{r(m)}$ is the coupling resonance wavelength of the m^{th} cladding mode,

$$n_{co}^{eff}(n_{co}, n_{cl}, \lambda) \quad \text{and} \quad n_{cl-m}^{eff}(n_{cl}, n_{sur}, \lambda)$$

are the effective refractive indices of the fundamental core mode and the m^{th} cladding mode; n_{co} , n_{cl} , and n_{sur} are the respective refractive indices of the core, the cladding, and the surrounding medium; Λ_{LPG} is the grating periodicity; and λ is the wavelength in free space. The guided core mode to cladding mode coupling in an LPG results in resonance at discrete wavelengths, which can be theoretically predicted by coupled-mode theory in conjunction with transfer-matrix

method [22]. The LPGs are fundamentally different from the well-known fiber Bragg gratings (FBGs) in that an FBG has an index perturbation period of half the irradiation wavelength (thus also termed short period grating), and in that it can couple light from the forward-propagating core mode to a backward-propagating core mode [23]. LPGs both in conventional fibers and in IG-PCFs are increasingly being developed for use as telecommunication components [24, 25] as well as for physical and chemical sensors [26-28].

LPGs in PCFs have been exploited for physical [29] and chemical sensors [30]. To date, documented PCF-LPG sensing schemes exclusively rely, at the fundamental level, on response to the changes in effective refractive indices of the core mode and coupled cladding mode through measurements of the transmission spectrum of the core mode. To take advantage of the unique microstructural and optical characteristic of PCFs and utilize the enabling feature of LPGs for cladding mode generation, we inscribe LPGs in PCFs to undertake core mode to cladding coupling for evanescent field sensing. The coupled cladding mode of low confinement loss at a prescribed resonance wavelength propagates in the air cladding along the fiber length and a transmission spectrum of the core mode is directly measured, which allows long interaction path length of the evanescent field of the cladding mode with analyte. The change of effective refractive index of cladding mode through evanescent field absorption by analyte shifts the resonance wavelength, offering excellent prospect of high detection sensitivity when implemented, but no selectivity in analyte of interest.

Our idea is to utilize the advantages from both PCF and LPG for chemical detection. In

order to fully explore the potential of PCF-LPG for evanescent field sensing with high sensitivity and selectivity, we have used two types of polymers as the nanofilm materials to be coated into air channels of the PCF cladding for coupled cladding mode transition. Two nanostructured polymer films are deposited at the surfaces of air channels in the PCF cladding by electrostatic self-assembly (ESA) deposition technique [31]. The primary nanofilm (the first coating) does not have a significant effect on PCF-LPG parameters such as grating resonance wavelengths and its intensity that can be used for sensing, but it increases the sensitivity to refractive index of chemical analytes in the air channels. The secondary nanofilm (the second coating) is used for selective absorption of analyte molecules of interest. These two nanofilms significantly modify the cladding mode distribution of PCF-LPG and enhance the evanescent wave interaction with the external environment, which builds a high sensitive and selective chemical sensor. As such, it is a good candidate as a humidity fiber sensor for applications in corrosion detection of SHM.

Chapter 1--Numerical Calculation for PCF Design

An optical fiber is a flexible, transparent fiber made of silica or plastic, with diameter of 250 μm with a plastic jacket. Functioning as a wave guide, optical fibers typically include a transparent core surrounded by a transparent cladding material with a lower index of refraction (the typical refractive index for the cladding and core are 1.52 and 1.62 respectively), which keeps the light confined in the core by total internal reflection. With the features of low signal loss and immunity to electromagnetic field interference, it has been widely used as a waveguide, to transmit light between the two ends of the fiber. Fibers that support many propagation paths or transverse light rays (modes) are called multi-mode fibers (MMF), while those that only support a single light ray (mode) are called single-mode fibers (SMF).

Photonic-crystal fibers (PCF), compared with traditional optical fibers, have the same external diameter with a plastic jacket, but contains rings of air channels in the cladding. This new generation of optical fibers not only has ability to confine light in hollow cores as a wave guide, but also can let gas or liquid chemicals pass through. With this feature, PCF is now finding applications in many application areas, especially in highly sensitive gas sensors.

For sensing purpose, a well-designed Index Guided- Photonic Crystal Fiber (IG-PCF) could directly improve sensitivity and optical requirements of guided-light systems by providing low loss and high mode intensity overlap with air channels in fiber cladding. The mode calculation gives us the mode intensity distribution in the fiber cross-section and the propagation constant $\beta = n_{\text{eff}}2\pi/\lambda$, indicating the optical phase (real β) and attenuation (imaginary β) that accumulates as

light propagates. For a given IG-PCF geometry, modal analysis needs to be performed so as to achieve necessary understanding and control of excitation with low-loss cladding modes at a desired resonance wavelength. To predict cladding modes that are likely to be coupled with the fundamental core mode for the IG-PCF LPG sensor, the basic criteria will be (1) large mode field overlap, (2) high coupling coefficient, and (3) minimum confinement loss for propagation in the grating region of the cladding.

1.1 Simulation theories and tools

Commercial software-MODE Solutions, which is a fully-vectorial mode solver combined with a frequency-domain method, is used to model the structures of IG-PCFs. The main objective of this work is to calculate the cladding mode overlap with air channels in IG-PCFs, the definition of which is the modal power fraction (PF) within the cladding air channels (the ratio of optical power inside the air channels to the total power) that can be calculated using the expression:

$$PF = \frac{\int_{A_c} S_z dA}{\int_{A_c} S_z dA} \quad (2)$$

where $S_z = \frac{1}{2} \text{Re}(E \times H^*) \cdot \hat{z}$, S_z is component of the Poynting vector, E and H are the electric and magnetic fields within the fiber cross-section respectively, \times denotes the vector cross product, \hat{z} is the unit vector along the fiber axis, \hat{z} is defined to be the infinite transverse cross-section, and C refers to integrating over the air channels.

1.2 Parameter chosen and numerical analysis

Two types of IG-PCFs, which consist of 5 rings of air-channel round latticed (denoted as IG-PCF A, see Fig. 1(a)) and hexagonal latticed (denoted as IG-PCF B, see Fig. 1(b)), respectively, were investigated. The average air-channel diameters (d) of IG-PCF A and B are $\sim 2.1 \mu\text{m}$ and $\sim 4.2 \mu\text{m}$, while the center-to-center distances (Λ) between the air channels in IG-PCF A and B are $\sim 3.3 \mu\text{m}$ and $\sim 6.5 \mu\text{m}$, respectively. Defining the core diameter (D_{core}) yields the relation $D_{\text{core}} = \Lambda(2 - d/\Lambda)$ and the values for IG-PCF A and B are $4.49 \mu\text{m}$ and $8.78 \mu\text{m}$, respectively. The outer diameters of the IG-PCFs match the typical value of $125 \mu\text{m}$. There are multi modes in the core for these two types of IG-PCFs because their air filling fractions (d/Λ) are larger than 0.428 (0.64 for IG-PCF A and 0.65 for IG-PCF B). A single-mode in the fiber is a necessary condition in sensing applications if the measured properties are interrogated using phase or wavelength encoding. Taking into account the reduction of propagating modes, we can tailor the IG-PCF geometries by means of a cladding with small air filling fraction and/or the decreasing of core size. The requirements for desired optical properties are found by numerical analysis in terms of a single mode pattern, a high intensity overlap with the air channels in cladding, and a large effective area in the core to make coupling easy.

The structures are modeled and the characteristics of fundamental core mode and higher order cladding modes are analyzed for the two geometrical IG-PCFs. Because of rotational symmetry for IG-PCF A and C_{6v} symmetry for IG-PCF B with arrayed air channels, it is noted that we can make the computation window in a quarter of the fiber cross-section



Figure 1. Cross-sectional optical micrographs of endlessly single-mode Index Guide-Photonic Crystal Fibers (IG-PCFs) (fabricated by Yangtze Optical Fiber and Cable Company Ltd.) with (a) 5 rings of air-channel round latticed in cladding and (b) 5 rings of air-channel hexagonal latticed in cladding section with a perfect electric and magnetic conductor boundary condition applied along symmetrical planes.

For a symmetrical IG-PCF mode, we can achieve accurate predictions in numerical computation by selecting an appropriate mesh spacing (grid size), which is certainly an important step. Acceptable results, with respect to the discretization scheme that has been used in the calculation, can be obtained by keeping the mesh spacing at $\sim \lambda/15$. The boundary condition is another critical factor for simulation of mode properties. We have employed an absorbing perfectly matched layer (PML) boundary condition for the truncation of computation domain without reflection. After PML parameters are discretized into mesh spacing, effective indices and field distributions of the fundamental core mode and higher order cladding modes can be calculated. Numerical results demonstrated the effectiveness of PML boundary condition.

1.3 Design results and discussion

Due to the fact that the air-channel structure in the cladding of an IG-PCF determines the optical properties of the fiber, which provides a large degree of freedom in tailoring the characterizations of the cladding modes through control of the geometries of air-silica cladding, three parameters are optimized in the simulation, including the number of air-channel rings, the distance between the consecutive air-channel rings and the diameter of air-channel, for air channels to provide ingress of analyte to the regions with a strong evanescent wave. The cladding modes with the maximum overlap rate in air-channel round and hexagonal latticed IG-PCFs, compared with typical Gaussian beam, have been recorded. The periodicities of LPGs have been calculated by phase-matching condition through setting the resonance wavelength in 1550 nm, which will be practically considered in the writing of LPGs, and also based on the light beam spot size using CO₂ laser for inscription. We have examined the percentage power overlaps with air channels for linear polarized core mode (LP₀₁) coupled to cladding modes (LP_{0m}), assuming that an LPG is inscribed in the IG-PCF, as the function of number of air-channel rings (4, 5, and 6), d (from 3 μm to 4 μm with interval of 0.2 μm), and Λ .

Table 1. Optimized parameters and overlaps of IG-PCFs with air channels round and hexagonal latticed.*

IG-PCF	LP _{nm}	$n_{eff(clad)}$	d (μm)	Λ (μm)	d/Λ	Number of rings	Λ_{LPG} (μm)	Overlap (%)
R**-1	LP ₀₄	1.4321	2.6	7.5	0.35	4	160.3	2.28
R-2	LP ₀₂	1.4399	2.8	7.0	0.40	5	1,230	4.01
R-3	LP ₀₉	1.4320	2.6	7.5	0.35	6	160.1	2.04
H***-1	LP ₀₂	1.4402	2.8	8.0	0.35	4	885.7	4.40
H-2	LP₀₂	1.4383	2.8	7.0	0.40	5	545.8	6.54
H-3	LP ₀₂	1.4399	2.6	7.5	0.35	6	870.8	2.39

* Numerical calculation at 1553.33 nm, refractive index between 1.45 and 1.40, cladding radius of 62.5 μm , and overlap compared with Gaussian beam.

** IG-PCF with air channels round latticed.

*** IG-PCF with air channels hexagonal latticed.

(from 7 μm to 9 μm with interval of 0.5 μm), based on $d/\Lambda < 0.42$ that is required for the characteristic of endlessly single mode in the IG-PCFs. Listed in Table 1 are the geometrical parameters of six optimized IG-PCFs (denoted as R-1, R-2, R-3, H-1, H-2, and H-3) for the m th-order of LP₀₁-LP_{0m} mode coupling with air channels round and hexagonal latticed in cladding, and for maximum overlaps for different number of air-channel ring. The LPG periodicities (Λ_{LPG}) satisfied by phase-matching condition are also listed in Table 1.

We have numerically calculated the first ten orders of cladding modes in a variety of IG-PCFs, in the claddings of which the air channels are round or hexagonal arrayed with 4-6 rings, and variable air-channel diameter as well as distance between two adjacent air channels.

By adjusting the above-mentioned parameters through calculation, we can obtain a cladding

mode whose mode field can be excited by the fundamental core mode with a LPG and maximally overlapped with air channels in cladding.

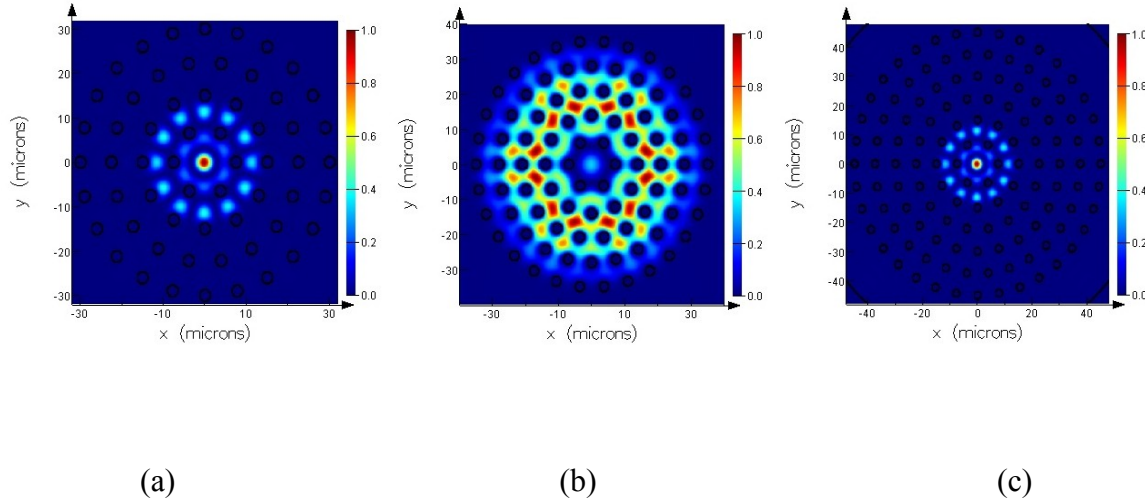


Figure 2. Transverse E_x intensity distributions of symmetric cladding modes with maximum overlap with air channels round latticed for: (a) 4 rings of air-channel (fiber R-1), (b) 5 rings of air-channel (fiber R-2), and (c) 6 rings of air-channel (fiber R-3).

Shown in Fig. 2 are the transverse E_x intensity distributions of symmetric cladding modes that clearly illustrate the overlap with round latticed channels. It is interesting that no matter how many number of air-channel rings are round latticed in cladding, the larger the air filling fraction (d/Λ in the range of endlessly single mode operation) is, the stronger the overlap is. This is because more coupled cladding mode power is extended to the interface of air channels as d becomes larger or Λ becomes smaller.

The confinement loss is another issue for the coupled cladding mode. It can also be seen from Fig. 2(a) that the lowest-order cladding mode (LP_{02}) has its mode field distributed over the

round pattern air-channel in the fiber cladding. In general, we select the LP₀₂ cladding for resonance coupling with the LP₀₁ core mode. As will be discussed in greater detail in Chapter 2, the LP₀₂ mode intensity distribution in the cladding provides the best overlap with the air-holes, leading to better analyte/light interaction. The LP₀₁ and LP₀₂ modes have the same symmetry and linear polarization that can maximize their coupling strength, leading to the largest overlap of intensity profile in terms of coupling coefficient (k^{1-2}) which can be expressed by

$$k^{1-2} = \frac{2\pi \langle \Delta n_{co} \rangle \eta^{1-2}}{\lambda} \quad (3)$$

where $\langle \Delta n_{co} \rangle$ is the cross-section average core index modulation of the IG-PCF and η^{1-2} is the overlap integral of LP₀₁ and LP₀₂ modes. As can be seen in Table 1, the IG-PCF with 5 rings of air-channel round arrayed has its largest overlap for the LPG periodicity of 1,230 μm . Compared to the overlap (0.11%) of the innermost ring of air channels round arrayed in cladding by directly using fundamental core mode, the LPG coupled cladding mode has its overlap with air channels up to 4.01%, improved by a factor of 36. The drawback is the long length of the IG-PCF LPG resulting from large grating periodicity, limiting their applications in which a short one is needed.

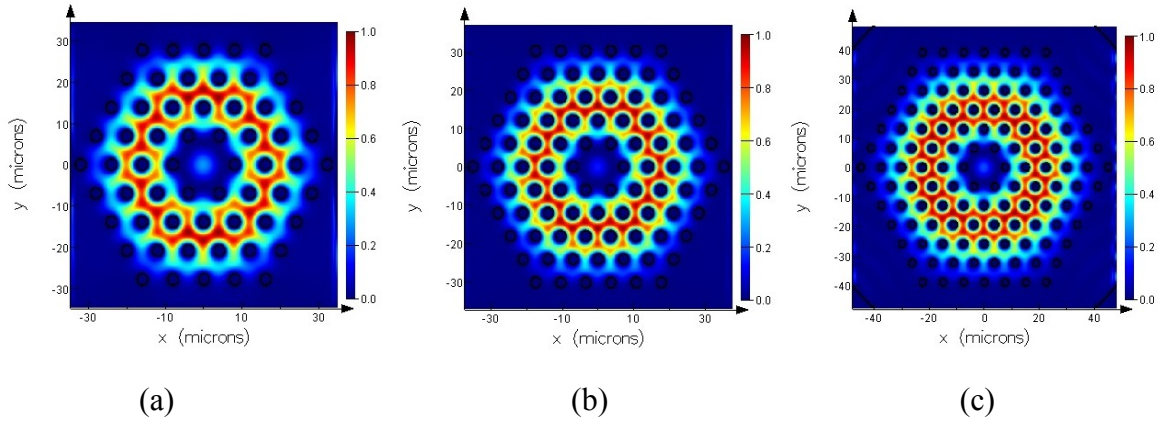


Figure 3. Transverse E_x intensity distributions of symmetric cladding modes with maximum overlap with air channels hexagonally latticed for: (a) 4 rings of air-channel (fiber H-1), (b) 5 rings of air-channel (fiber H-2), and (c) 6 rings of air-channel (fiber H-3).

Shown in Fig. 3 are the transverse E_x intensity distributions of symmetric cladding modes that clearly illustrate the overlap with hexagonally latticed air channels. Note that all LP_{02} cladding modes possess maximum overlaps with air channels. On the other hand, the LP_{02} cladding mode in fiber H-2 has its strongest coupling strength, with the highest overlap that is highlighted with red color in Table 1. In contrast to what might be expected, more air channels in cladding, or simply increasing of air-channel ring, cannot provide higher evanescent wave overlap. The most important parameter to note is the accumulated intensity at the surface of air-silica, which contributes to the strength of evanescent wave.

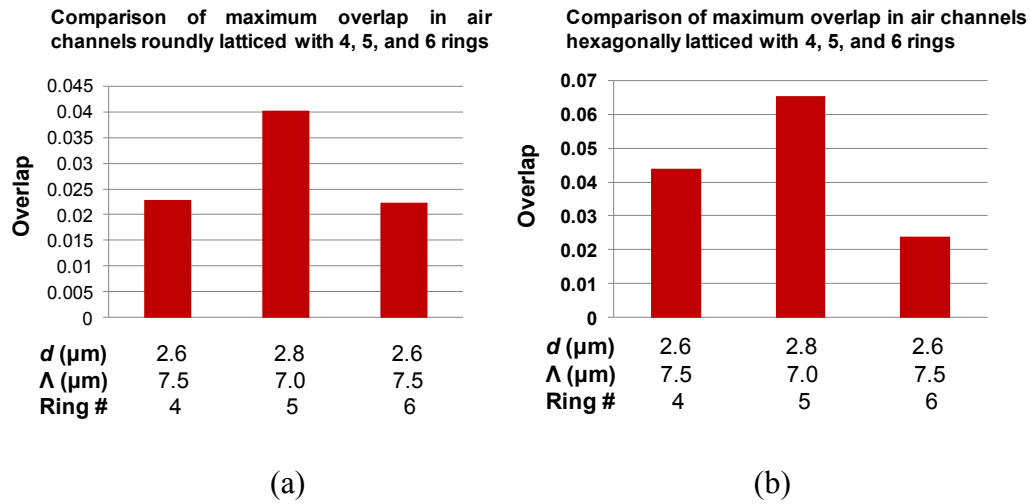


Figure 4. Comparison of maximum overlap in air-channel with different parameters (d , Λ , and number of air-channel rings): (a) air channels in cladding are round arrayed and (b) air channels in cladding are hexagonally arrayed.

Displayed in Fig. 4 is the comparison of maximum overlap in air-channel with different fiber parameters. This figure gives a set of IG-PCF fabrication-oriented geometry parameters that optimize the coupled cladding mode by a LPG with a suitable periodicity, and give rise to a strong overlap with air channels in the cladding for evanescent sensing. It can be concluded, from our simulation results, that the fabrication of IG-PCF is most likely processed with fiber diameter of $2.8 \mu\text{m}$, distance between two air channels (center-to-center) of $7 \mu\text{m}$, ring number of air-channel in cladding of 5, and the periodicity of $545.8 \mu\text{m}$ of the LPG that is inscribed in the fiber. With these parameters, we note that the overlap of the designed fiber is as high as 6.54% ,which is 50 times higher than that provided by directly using the fundamental core mode.

Chapter 2--LPG principles and its fabrication on PCF

2.1 Modes in PCF for evanescent field sensing

It is worth noting that other fiber-optic platforms have been explored for vapor phase and/or aqueous solution sensing with evanescent field of a guided light or direct laser excitation. While simple design and implementation are carried out, the schemes utilizing conventional optical fiber with its cladding or even part of its core removed (as in the case of D-shaped fiber) are typically limited by the probe length (a couple of centimeters due to potential compromise in mechanical and structural integrity) and mechanical strength. The specific surface is also limited for evanescent field intensity-analyte interaction in such probe geometries although relatively high field intensity overlap is possible in some D-shaped fiber designs. Compared to their conventional optical fiber counterpart, PCFs are a particularly attractive sensing platform because the vapor/fluid can be entered into the air channels directly and, furthermore the fiber-optic characteristics can be optimized to improve sensitivity.

The fundamental core mode in the PCF has been used for evanescent field sensing. While this sensing modality has demonstrated its potential for sub-monolayer measurements, there exist two inherent limitations. First, the evanescent field extends only a small distance ($\sim \lambda/3$, λ is the operating wavelength) from the guiding core to the surrounding PCF cladding air channels, restricting the analyte and light interaction region to only the innermost ring of air channels in the cladding. Secondly, the fundamental core mode is localized mostly in the PCF core and, in fact, for most designs, less than 1% power of the core mode overlap with the surrounding air

channels thus providing weak light intensity-analyte interactions for spectroscopic interrogation.

Shown in Fig. 5 are the numerical simulations for the linear polarization (LP) mode field intensity distributions of a PCF LP_{01} fundamental core mode and cladding modes from LP_{02} to LP_{07} at wavelength of 1550 nm, including states of degeneracy, as in Fig. 5(c) and (g) shown. As shown in Fig. 5(a) in the case of LP_{01} , the mode field overlap with air channels is limited to only 0.13% of the core mode for the traditional approach of evanescent field sensing using PCF. The overlap becomes weaker and weaker from LP_{03} to LP_{07} cladding mode, [Fig 5(c) to (g)]. The LP_{02} cladding [Fig. 5(b)], however, exhibits the strongest and broadest intensity field overlap, $\sim 4.40\%$. Should the LP_{02} cladding mode be selectively excited using a LPG and utilized for sensing, it would drastically enhance the sensitivity of evanescent field interaction, and this is the approach taken here.

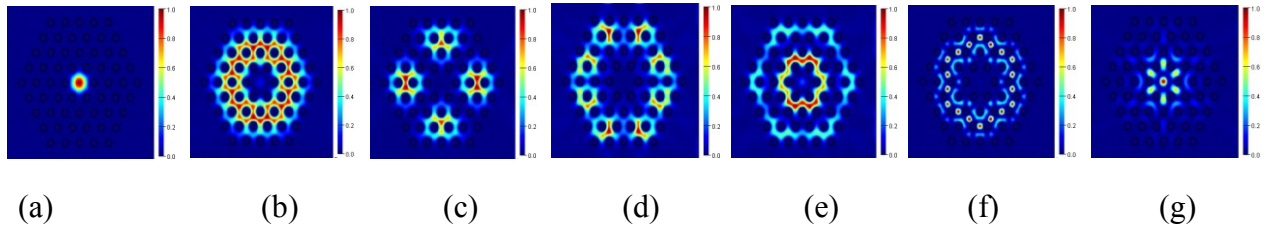


Figure 5. Linear polarization (LP) mode field intensity distributions in a PCF with 4 rings of air-channels hexagonally arranged, calculated at wavelength of 1550 nm for: (a) LP_{01} fundamental core mode, (b) LP_{02} cladding mode, (c) one state of degeneracy in LP_{03} cladding mode, (d) LP_{04} cladding mode, (e) LP_{05} cladding mode, (f) LP_{06} cladding mode, (g) one state of degeneracy in LP_{07} cladding mode.

2.2 Phase-matching condition and Coupled-mode theory

A Long Period Grating couples the fundamental core mode to several co-propagating cladding modes in a single mode fiber, resulting in a sequence of attenuation resonances in the transmission spectrum. The LPG is an intrinsic and passive device that can be induced by a periodic refractive index modulation in the fiber core with a typical period of a few hundred micrometers. Four parameters in a LPG can be described as follows: $\lambda_{(i)}$, the resonance wavelength of the i^{th} linear polarization cladding mode (LP_{0i}); $n_{\text{eff,core}}$ and $n_{\text{eff,clad}(i)}$, the effective indices of the fundamental core mode and the i^{th} cladding mode; and $\Lambda(L)$, the periodicity of the grating, and the relationship of which can be expressed by

$$\lambda_{(i)} = (n_{\text{eff,core}} - n_{\text{eff,clad}(i)}) \Lambda(L) \quad (4)$$

and their transmission spectra are characterized by resonance bends at wavelengths that satisfy the phase-matching condition. The LPGs in both conventional optical fibers and PCFs have been used as transducers for environmental sensing such as temperature, strain, vibration, and chemical measurements.

Coupled-mode theory can be applied to calculate the intensity of resonance in LPGs, which is determined by the coupling coefficient κ and the grating length L [32]. The minimum transmission is proportional to $\cos^2(\kappa L)$, while the coupling coefficient is a function of the effective index change and the mode overlap between the guided core mode and the coupled cladding mode over the region of refractive index change. The surrounding material will affect the coupling. In the next section, the resonance spectrum obtained in our PCFs is compared with

the simulations using coupled-mode theory.

2.3 Fabrication of LPGs in PCF

The fibers which we used to inscribe LPGs are the endlessly single mode PCF (ESM-PCF, simply called as PCF). The specifications for PCF used here are: the center-to-center distance between the air channels (Λ) is $6.4 \mu\text{m}$; the average air-channel diameter (d) is $3.1 \mu\text{m}$; the d/Λ is 0.48. The channels are arranged in a hexagonal pattern, extending to a diameter of $65 \mu\text{m}$. Defining the core diameter (D_{core}) as $D_{\text{core}} = \Lambda(2 - d/\Lambda)$ leads to a value of $10.4 \mu\text{m}$. The outer diameter of the PCF matches the typical value of $125 \mu\text{m}$ as for most of SMF fibers.

A melt fiber preform is drawn into the size of a normal fiber diameter during the fiber drawing process. Tension, which is called mechanical residual stress, is accumulated in the fiber core with frozen silica in the cladding by radial variations of viscoelasticity and thermal expansion because of temperature gradient in the fiber drawing furnace. The residual stress in the fiber core influences the refractive index of that area by the photoelastic effect, and it can be released at the softening temperature of silica by a focused pulsed beam from a CO_2 laser. Periodic irradiation of CO_2 laser beams on the fiber results in the stress relaxation with the desired grating-pattern. A change of refractive index ($\sim 10^{-3} - 10^{-4}$) in the core can be achieved to form the LPGs in the fiber.

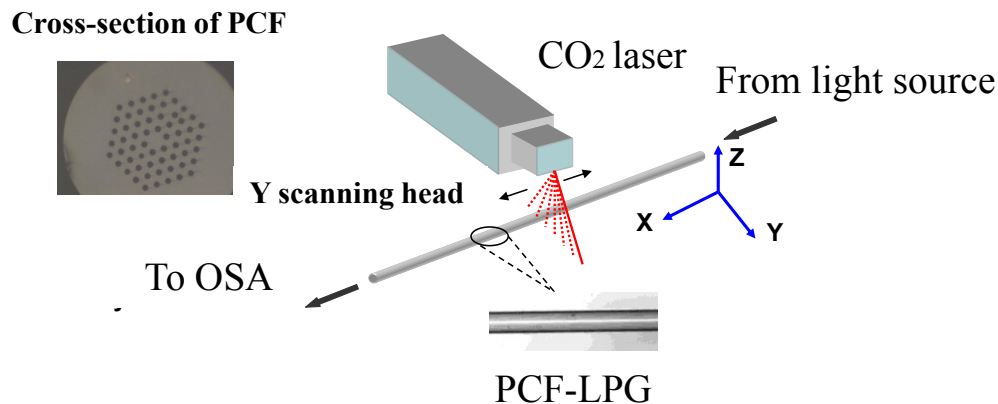


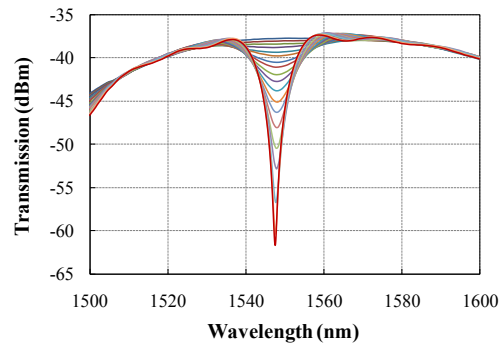
Figure 6. Schematic diagram of experimental setup for LPG inscribed in PCF by focused beam of CO₂ laser with a 1-D galvanometer (the insets are the cross-sectional optical micrograph of PCF and the outlook of PCF-LPG).

Shown in Fig. 6 is the experimental setup for fabrication of LPGs. The insets of this figure are the cross-sectional optical micrograph of PCF and the outlook of PCF-LPG, respectively. The LPG fabrication system includes a CO₂ laser with a 1-D galvanometer. The laser beam is passed through a ZnSe cylindrical lens with a focal length of 198 mm, and located on the 1-D galvanometer that focuses and directs the beam diameter to a $\sim 150 \mu\text{m}$ Gaussian focal spot on the fiber. The fiber is held by positioners whose movement can be controlled by a translation stage attached to them.

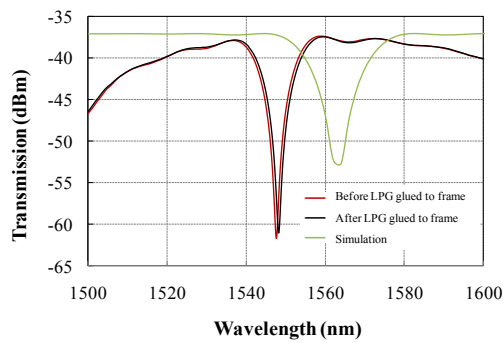
One end of the fiber is connected to a broadband superluminescent light-emitting diode (SLED) light source with total power of 9.25 mW, while other end of the fiber is connected to an optical spectrum analyzer (OSA) with wavelength region from 1450 nm to 1650 nm for

analyzing the transmission spectrum profile of the LPG in situ. A point-by-point technique is employed to localize the laser heating at periodic intervals on the fiber. As the fiber is moved to each new position by the translation stage, the CO₂ laser is turned on and the laser beam is incident on the fiber for a preset amount of exposure.

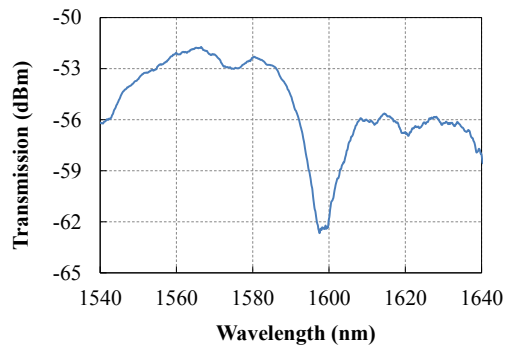
The transmission characteristics of the LPG can be measured during grating inscription. Shown in Fig. 7(c) is the transmission spectrum of the PCF-LPG with 69 periodicities, each length of which is 420 μm , and resonance wavelength of 1597.10 nm.



(a)



(b)



(c)

Figure 7. (a) Transmission spectra of the SMF-28-LPG with periods from 40 to 115 at interval of 5-period increase, (b) transmission spectra of the SMF-28-LPG before and after bonded to the RH testing frame as well as the simulated grating spectrum, and (c) transmission spectrum of PCF-LPG at resonance wavelength of 1597.10 nm with 69 periods.

The quality of LPG used as a chemical sensor can be defined by its full-width at half maximum (FWHM) of transmission resonance profile. The more grating periods the LPG has, the smaller the FWHM is. In other words, the narrower the resonance dip of the LPG, the higher the sensitivity of a fiber will be. We have fabricated the PCF-LPGs whose FWHM are around 2 nm. Compared to the PCF-LPGs that Rindorf et al. have inscribed [33], we have smaller value of FWHM but the property of our PCF-LPG in terms of sensitivity still can be improved through the following techniques and methods: (1) we can use rotational state that enables us to rotate PCF for CO₂ laser three-side exposure instead of one-side exposure, which could uniformly cylindrical refractive index change; (2) we can design the different geometrical PCFs so that those PCFs have larger contrast of refractive index between core and air-hole cladding.

2.4 Sensing mechanism

The robust nature of PCFs as a platform for evanescent field sensing and detection of analytes has been demonstrated, which stems from evanescent field interaction of guided core mode with the analyte in the cladding air channels over a long path length. In addition, the accessibility of gas/liquid inside the air channels makes it possible to functionalize the air channels for higher detection sensitivity and selectivity. Yet, far greater detection sensitivity and selectivity can be achieved than currently explored core mode evanescent sensing modality if we can generate and use strong cladding modes that interact with the entire air cladding of the PCF. As the cladding of a PCF has a small and finite area further confined by a solid outer layer,

cladding modes coupled with the core mode can propagate with low confinement loss.

The cladding modes of PCFs have been theoretically analyzed to predict the coupling between LP_{01} core mode and HE_{11} cladding mode in a PCF-LPG with high accuracy.[10] We have used the MODE Solutions method to numerically predict cladding modes that are likely to be coupled with the fundamental guided core mode.

The basic criteria will be (1) high coupling coefficient, (2) large mode field overlap, and (3) minimum confinement loss for propagation in cladding. As discussed in the previous chapter, we have conducted a simulation of a LPG on PCF, which has 5 rings of air-channel in cladding, with a grating periodicity of $670 \mu\text{m}$ and grating length of 14 periods ($\sim 0.94 \text{ cm}$). The analysis was specifically performed on LP_{04} cladding mode coupling with LP_{01} fundamental core mode of the LPG in the PCF. Shown in Fig. 8(a), (b), (c), and (d) are calculated power distribution in amplitude and phase of LP_{04} in the hexagonal region of two orthogonal degeneracy

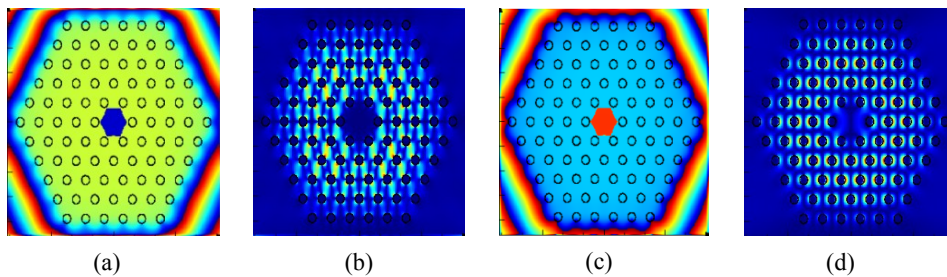


Figure 8. Simulated power distributions of LP_{04} cladding mode in PCF excited by a LPG (periodicity of $670 \mu\text{m}$ and period number of 14): (a) EX in amplitude, (b) EX in phase, (c) EY in amplitude, and (d) EY in phase birefringence of EX and EY, respectively.

The PCF-LPG was calculated to exhibit a resonance of -23 dB at wavelength of 1550 nm and a confinement loss of 2.4 dB/cm. The analysis indicates that, for a given cladding symmetry, air-channel size, and channel-to-channel separation, confinement loss of LP_{04} cladding mode decreases exponentially with the number of rings of the air channels. The confinement loss of cladding modes is also a function of cladding microstructure. The numerical simulations clearly offer a powerful means of predicting and understanding the mode characteristics of a given PCF-LPG configuration and ultimately the design and fabrication of optimal PCF structures for LPG excitation of cladding mode coupling.

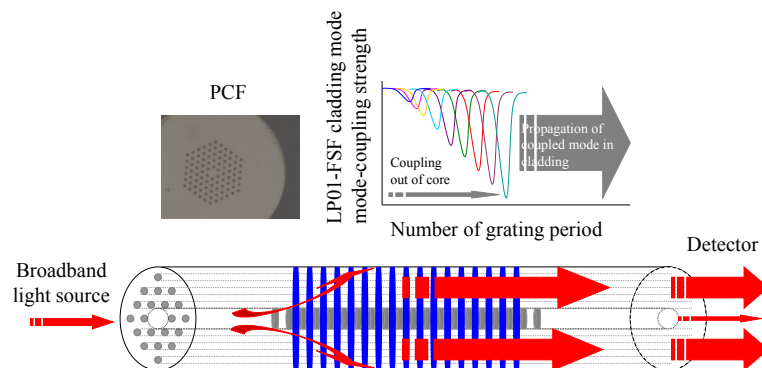


Figure 9. Schematic diagram of core-to-cladding mode coupling in a PCF-LPG structure (the top-left inset is the cross-sectional optical micrograph of PCF, and the top-right inset illustrates that the mode coupling resonance strength depends strongly on the grating design with the number of grating periods being an important parameter).

Illustrated in Fig. 9 is the schematic diagram for core-to-cladding mode coupling in a PCF-LPG structure. The top-left inset is the cross-sectional optical micrograph of PCF that has been used in the experiments, while the top-right inset displays the mode coupling resonance strength which depends strongly on the grating design with the number of grating periods. The working principle of core mode and cladding modes coupling in a PCF-LPG is based on coupled-mode theory and phase-matching condition. The resonance intensity corresponds to the amount of power transferred to the coupled cladding mode at the resonance wavelength. It is a function of number of grating periods. The total power oscillating between the fundamental core mode and the coupled cladding mode is proportional to the minimum transmission which is given by:

$$T_{\min} = 1 - \sin^2(KL) \quad (5)$$

where, K is the coupling coefficient of the cladding mode and L is the grating length.

Chapter 3--Nano film coatings and its deposition on PCF

3.1 Nano films and its coating

It is desirable to incorporate nanostructure films into LPG to enhance sensitivity and selectivity. Indeed, a LPG deposited with high refractive index (higher than refractive index of fiber cladding) nanostructure material was first reported for a better understanding of dependence of resonance wavelengths on the optical thickness of the nanofilm [34]. More detailed works have also been reported on thin nanofilm-coated LPs, describing the effects of high refractive index coating on sensitivity of coated LPG to the change of external refractive index, and finding a large resonance wavelength shift that permits the sensitivity of coated LPG sensor to be significantly improved [35-43].

Improvement of sensitivity and selectivity of the PCF-LPG sensors is a critical challenge in the field of the detection of chemical analytes. To this end, we have coated two types of nanostructure polymer films, in which refractive index of the first nanofilm is higher than that of silica and refractive index of the second nanofilm is lower than that of silica, into the surfaces of air channels in the PCF-LPG. The new cladding mode is created and bounded within the first nanofilm that determines the change in the power distribution of cladding modes and their effective refractive indices. Because of the mode transition, the greater part of light intensity of the lowest order of cladding mode moves to the first nanofilm, in which the evanescent field is drastically enhanced and the effective refractive index of the cladding mode is increased. As a result, the sensitivity of the PCF-LPG can be improved in terms of resonance wavelength shift

and transmission intensity in response to change of external refractive index. The second nanofilm is able to interact specifically with water molecule by absorption, and it exhibits high selectivity. In this work, we use the polymer of PAH⁺/PAA⁻ as the first nanofilm and Al₂O₃⁺/PSS⁻ as the second nanofilm to be coated on the surfaces of air channels in the PCF-LPG with ESA deposition technique. The developed nanofilm-coated PCF-LPG humidity sensor is useful for corrosion detection in structural health monitoring (SHM) applications.

3.2 ESA deposition process

We have employed Electro-Static Assembly technique to deposit the nanostructure coating onto LPGs for the enhancement of sensitivity and selectivity. The ESA deposition is one of the most powerful processes for assembling of polymer monolayer and/or multilayer because the thickness can be controlled with nano-scale precision. The operating principle of the ESA technique is straightforward. In our case, two oppositely charged polyelectrolytes that are suspended in water will attract. Due to the fact that the electrostatic interactions have a longer range than that of hydrophobic effects, the assemblies that can be built up electrostatically by attraction of polyelectrolytes can extend over a substantial range.

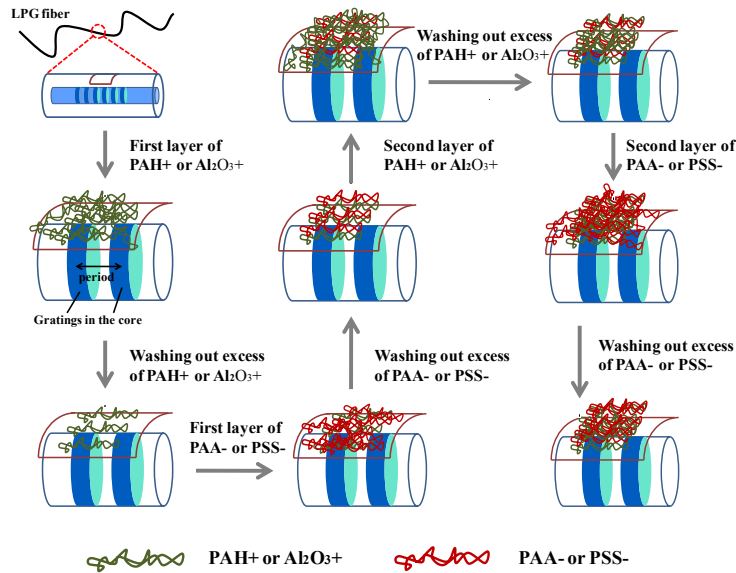


Figure 10. Schematic illustration of ESA deposition processing with PAH⁺ or Al₂O₃⁺ (positive charge) water solution and PAA⁻ or PSS⁻ (negative charge) water solution for LPG nanostructure coatings[44].

Show in Fig. 10 is a schematic illustration of ESA deposition processing by using polyallylamine hydrochloride (PAH⁺) or alumina (Al₂O₃⁺) with positive charge in solution and polyacrylic acid (PAA⁻) or poly-sodium 4-styrenesulfonate (PSS⁻) with negative charge in solution. The first step is that the region of LPG is rinsed with Milli-Q water to have a negatively charged fiber surface and sequentially immersed into PAH⁺ solution (5wt% in Milli-Q water) for 3 min, and then it is rinsed with Milli-Q water for 1 min to remove the polymer molecules that do not contribute to the monolayer nanostructure. The next step is that the rinsed fiber is

immersed into PAA- solution (3 wt% in Milli-Q water) for 3 min, and then rinsed again with Milli-Q water for 1min for the same purpose as previous one. After repeating those two steps 10 times, 10 bi-layers of PAH+/PAA- are deposited onto the fiber surface. The refractive index of PAH+/PAA- is 1.5526, and this coating with higher index than fiber cladding is used for the enhancement of sensitivity through cladding mode transition.

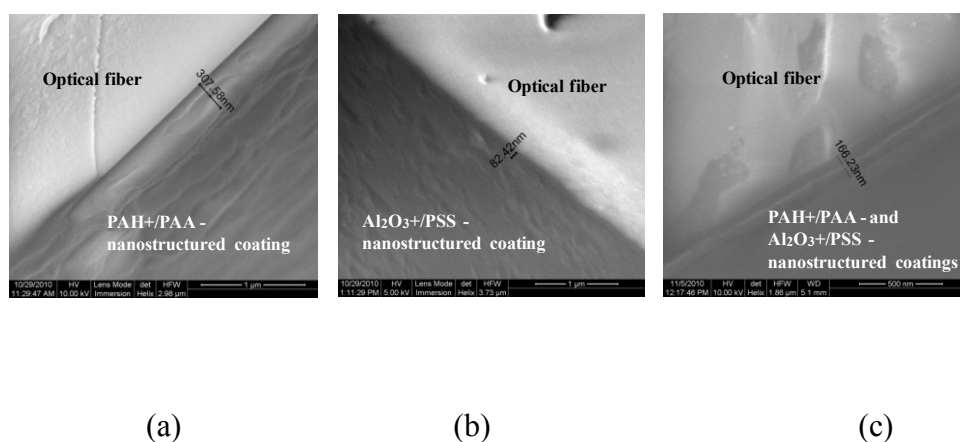


Figure 11. SEM images of nanostructure coatings on optical fiber: (a) PAH+/PAA- (10 bi-layers), (b) Al_2O_3 +/PSS- (10 bi-layers), and (c) PAH+/PAA- (5 bi-layers) and Al_2O_3 +/PSS- (5 bi-layers).

The scanning electron microscope (SEM) observations of the nanostructured coatings on LPG have been carried out in order to investigate their structure and thickness. Shown in Fig. 11(a) is a SEM image of PAH+/PAA- multilayer (10 bi-layers) with thickness of 307.58 nm. The average bi-layer thickness of this coating is around 30.8 nm. For Al_2O_3 +/PSS- nanocoating, the thickness of 10 bi-layers is 82.42 nm (see Fig. 11(b)) and one bi-layer thickness is ~ 8 nm. The

slight roughness of those two nanocoatings reveal that there are some impurities in the polymer surfaces. Fig. 11(c) shows that two types of nanocoatings (PAH⁺/PAA⁻ and Al₂O₃⁺/PSS⁻) are deposited on the optical fiber with total thickness of 166.23 nm that is thinner than the value of average thickness of PAH⁺/PAA⁻ plus average thickness of Al₂O₃⁺/PSS⁻ because the thicknesses of multilayers are scaled at SEM with different angles with respect to the facet of optical fiber. The purpose of PAH⁺/PAA⁻ nano-film deposited on the LPG section is to increase the sensitivity, while the Al₂O₃⁺/PSS⁻ nano-film is attributed to the water molecular absorption for humidity sensitivity.

3.3 Deposition on internal air channels of PCF----simulation and experiments

To deposit the nanofilms into the surfaces of air channels in the PCF cladding, we need to fill the air channels with polymer solution by means of layer-by-layer ESA method. In order to determine the length of time it takes for the solution to pass through a given length of PCF by capillary force, we use a capillary filling model to numerically calculate the dependence of time on length of PCF with a given geometry under different pressure.

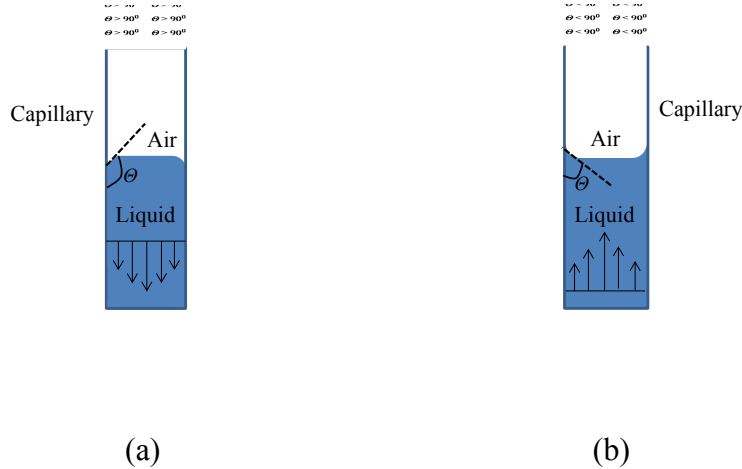


Figure 12. Schematic diagram of capillary tube with liquid inside and contact angle: (a) the liquid is pushed out of the capillary by capillary force with contact angle large than 90° and (b) the liquid is pulled into the capillary by capillary force with contact angle smaller than 90° .

Shown in Fig. 12 is the schematic diagram of capillary tube with liquid inside and contact angle between the rim of the liquid and the wall of capillary. The capillary force can push the liquid out of the capillary when the contact angle is larger than 90° (see Fig. 12(a)), while the capillary force can pull the liquid into the capillary when the contact angle is smaller than 90° (see Fig. 12(b)). The height of a liquid column in capillary by capillary force is given by:[13]

$$h = \frac{2\gamma \cos \theta}{\rho g r} \quad (6)$$

where γ is the liquid-air surface tension, θ is the contact angle, ρ is the density of liquid, g is local

gravitational field strength, and r is the radius of capillary. For a water-filled glass in air at standard laboratory condition, $\gamma = 0.0728$ N/m at 20 °C, $\theta = 0.35$ rad, ρ is 1000 kg/m³, and $g = 9.81$ m/s², and $r = 0.002$ mm, the height of the water column is about 3.7 m, but it is impractical to reach this height because it takes a long time. We therefore use a pressure differential between the two ends of the PCF to shorten the capillary filling time.

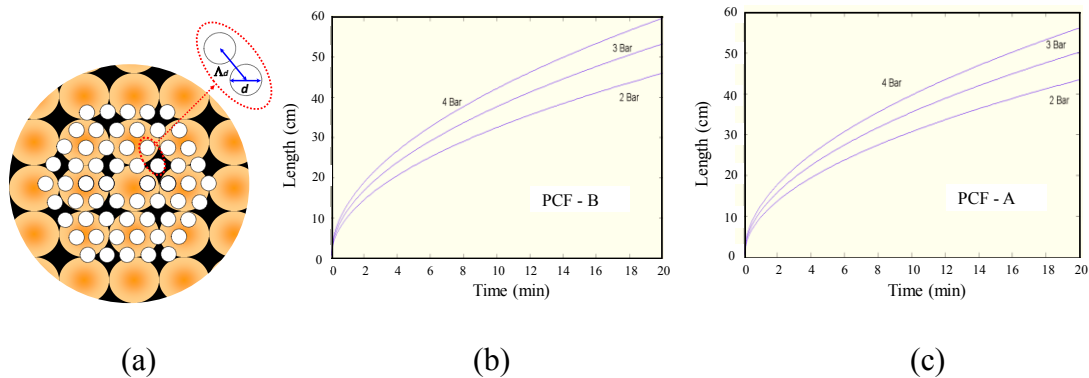


Figure 13. (a) Diagram of a cross-sectional PCF with 4 rings of air-channel in cladding (d : diameter of air-channel and Δd : distance of channel-to-channel separation), (b) numerically calculated water filling time of air channels in different length of PCF-A with d of 3.76 μm and Δd of 8.99 μm at pressure differences of 2 bar, 3 bar, and 4 bar, and (c) numerically calculated water filling time of air channels in different length of PCF-B with d of 4.23 μm and Δd of 8.07 μm at pressure differences of 2 bar, 3 bar, and 4 bar.

Water/solution flow in air channels of PCF is induced by a constant positive pressure difference, which can be modeled using Poiseuille flow [45]. For an air-channel PCF with diameter of d , length of l , water viscosity of η , and in the presence of a uniform pressures

difference of Δp , the water flow rate can be expressed by:

$$Q = \frac{\pi d^4 \cdot \Delta p}{128 \eta l} \quad (7)$$

For example, at Δp of 5 bar, it takes only 1.2 minutes for water to fill in an air channel (diameter of 4 μm) of 1-meter PCF. We have numerically calculated the water filling time of PCF air channels with the pressure difference of 2 bar, 3 bar, and 4 bar. Two types of PCF geometrical parameters were used with d of 3.76 μm and Δd (distance of channel-to-channel separation) of 8.99 μm in PCF-A and d of 4.23 μm and Δd of 8.07 μm in PCF-B. Shown in Fig. 13(a) is the diagram of a cross-sectional PCF with 4 rings of air-channel in cladding. From Fig. 13(b) and (c), it can be clearly seen that, the larger the diameter of air channel, the longer the filling length at the same filling time, which is also experimentally confirmed.

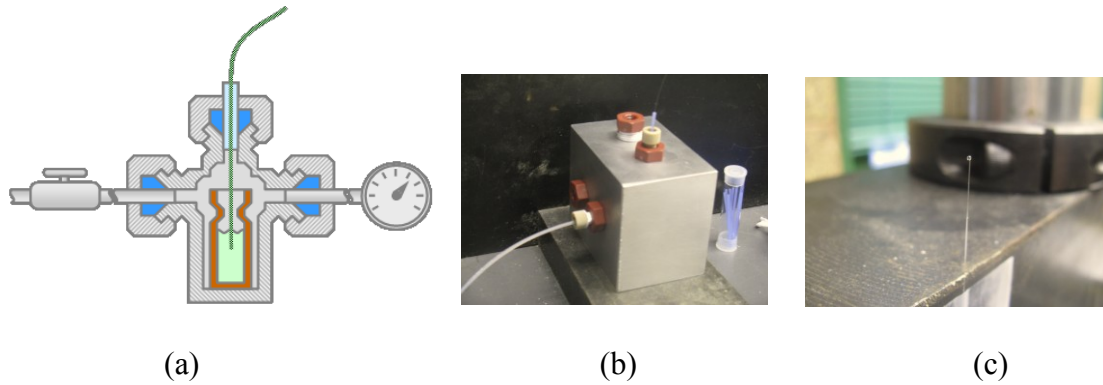
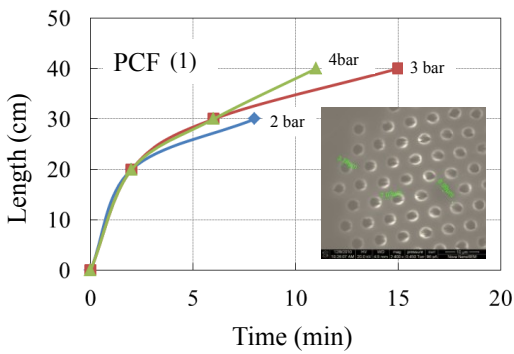


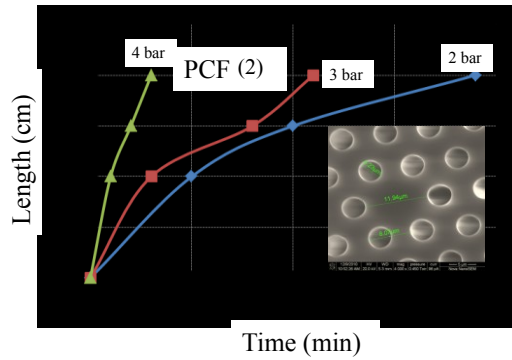
Figure 14. (a) Schematic of compressed air pressure chamber for the filling of water/polymer solution, (b) picture showing a compressed air pressure chamber that can fill two PCFs simultaneously, and (c) picture showing a drop of water out of air channels of the PCF.

Depicted in Fig. 14(a) is the schematic of compressed air pressure chamber that houses the flow entrance end of the PCF and a vial that contains water/solution. Fig. 14(b) shows the compressed air pressure chamber made with stainless steel, which can fill two PCF with water/solution simultaneously. The dimension of the chamber is $75 \text{ mm} \times 52 \text{ mm} \times 50 \text{ mm}$. Fig. 14(c) shows a drop of water coming out of the air channels of the PCF, the length of which is 600 mm. Two PCFs (PCF (1) and PCF (2)) with different geometrical parameters are used for pressurized water filling experiments. The PCF (1) has an air-channel diameter of $3.76 \text{ }\mu\text{m}$, air-channel to air-channel distance of $7.03 \text{ }\mu\text{m}$, and core diameter of $8.99 \text{ }\mu\text{m}$, while the PCF (2) has an air-channel diameter of $4.23 \text{ }\mu\text{m}$, air-channel to air-channel distance of $8.07 \text{ }\mu\text{m}$, and core

diameter of 11.94 μm . SEM images of cross-sections of PCF (1) and PCF (2) are shown in the insets of Fig. 8(a) and (b), respectively. Fig. 8(a) and (b) show the respective dependence of pressurized water filling time on filling lengths of PCF (1) and PCF (2) under pressures of 2 bar, 3 bar, and 4 bar. It can be seen that, at pressure of 2 bar, it takes longer time for PCF (2) than PCF (1) to fill the water into air channels with the same length because the friction force dominates the entire flow mechanism. Meanwhile, there is no clear difference of the filling length below 5 minutes with pressures of 2 bar, 3 bar, and 4 bar in PCF (1). At higher pressure, much less filling time is needed in PCF (2) than in PCF (1) for filling water into a given length of air channels. For example, it takes 3 minutes and 11 minutes to fill water into a length of 40-cm PCF (2) under pressures of 4 bar and 3 bar, respectively, but under the same pressures it takes about 11 minutes and 15 minutes, respectively, to fill the same length of PCF (1). In this work, we will use 4 bar or higher pressure for filling of polymer solutions in the experiments.

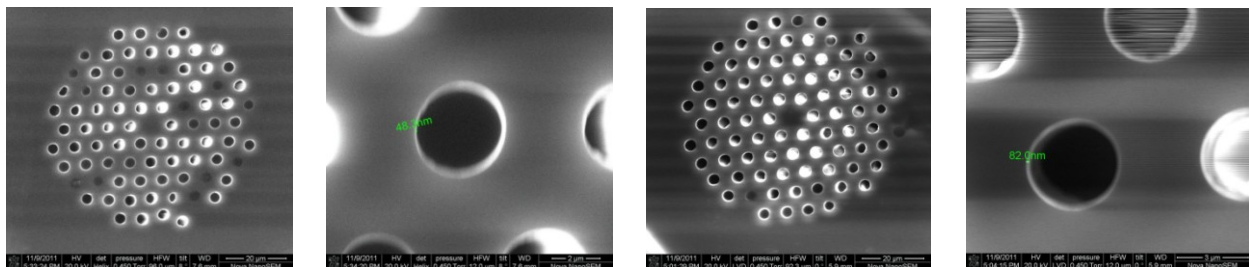


(a)



(b)

Figure 15. Dependence of pressurized water filling time on filling length with different pressure for (a) PCF (1) with air-channel diameter of $3.76 \mu\text{m}$, air-channel to air-channel distance of $7.03 \mu\text{m}$, and core diameter of $8.99 \mu\text{m}$ (the inset is the SEM image of PCF (1) cross-section) and (b) PCF (2) with air-channel diameter of $4.23 \mu\text{m}$, air-channel to air-channel distance of $8.07 \mu\text{m}$, and core diameter of $11.94 \mu\text{m}$ (the inset is the SEM image of PCF (2) cross-section).



(a)

(b)

(c)

(d)

Figure 16 SEM images for (a) cross-section of nanofilm-coated PCF with PAH⁺ and PAA⁻, (b) thickness of 3 bi-layers of PAH⁺ and PAA⁻, (c) cross-section of nanofilm-coated PCF with Al₂O₃⁺ and PSS⁻, and (d) thickness of 5 bi-layers of Al₂O₃⁺ and PSS⁻.

3.4 Nanofilms deposition and characterization

To coat the nanofilms on the fiber surface by ESA technique, it needs to be exposed to cationic and anionic solutions. Since the nanofilms are to be created in the inner surface of air channels of a PCF, a compressed air pressure chamber, as seen in Fig. 14(b), was used to force the polymer solution through the air channels. A 60-cm long PCF was inserted into the chamber with a vial containing Milli-Q water for washing the surface of air channels. After cleaning, the surface of air channels was negatively charged. The Milli-Q water in the chamber was removed and replaced by positively-charged PAH⁺ solution. After seeing a drop of the solution at the end of the PCF and waiting for 3 minutes, we removed the fiber from the chamber, and replaced Milli-Q water in order to wash the excess of PAH⁺ polymer molecules. Then a negatively-charged PAA⁻ solution was forced into the air channels, and the same deposition procedure was repeated. The consecutive layers of positively- and negatively-charged polymers are called bi-layers. Several bi-layers of PAH⁺/PAA⁻ were deposited first for the primary coating. Then, another type of bi-layer of Al₂O₃⁺/PSS⁻ was deposited several times using the bi-layers of PAH⁺/PAA⁻ as the secondary coating. Shown in Fig. 16 are the Scanning Electron Microscope (SEM) images for (a) cross-section of nanofilm-coated PCF with PAH⁺ and PAA⁻, in which some air channels are blocked due to the residue of PAH⁺/PAA⁻ polymerization; (b) thickness of 3 bi-layers of PAH⁺ and PAA⁻ (48.3 nm); (c) cross-section of nanofilm-coated PCF with Al₂O₃⁺ and PSS⁻; and (d) thickness of 5 bi-layers of Al₂O₃⁺ and PSS⁻ (82.0 nm). A slight roughness of the nanofilms is observed because of the formation of polymer chain. The thickness of the

nanofilm can be precisely controlled by the number of the deposited bi-layer, while the polymeric materials of nanofilms are determined by the chemical detection that is based on the change of a property of the sensing material as a consequence of sorption and desorption of a specific analyte. The properties of the nanofilms make themselves not only sensitive but also selective to water molecules.

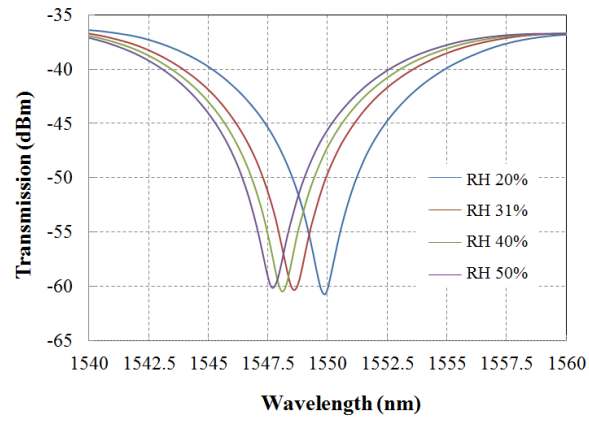
Chapter 4-- RH testing results and discussion

4.1 RH response of SMF-28-LPG

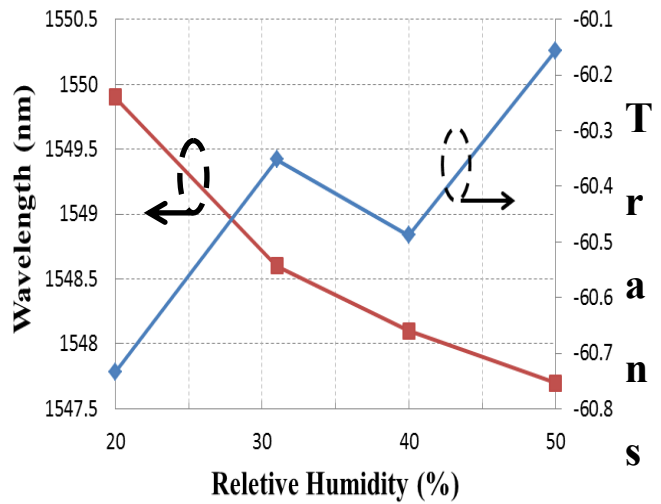
We first compared the humidity sensitivity of SMF-28-LPG to that of nanofilm-coated SMF-28-LPG in a humidity chamber that includes a mini ultrasonic humidifier, a digital temperature/humidity meter, and the sensor which was fixed on a plastic frame to eliminate mechanical bending as shown in Fig. 17. Fig. 18(a) shows that when the RH increases from 20% to 50% at room temperature, the resonance wavelength shifts toward blue side (short wavelength) from 1549.9 nm to 1547.6 nm while the transmission intensity slightly increase from -60.734 dBm to -59.873 dBm, which are plotted in Fig. 18 (b). The resonance shift to smaller wavelength is because the larger the RH the higher surrounding refractive index, which causes a smaller difference of effective refractive indices of the core mode and the coupled cladding mode. The coefficient of the grating sensitivity to RH with respect to wavelength shift is about 0.0136%/pm, and the coefficient of sensitivity in terms of intensity difference is 0.0519%/10⁻³dBm.



Figure 17: Humidity chamber with the LPG fiber sensor fixed on a plastic frame, the moisture generator, and the humidity-meter.



(a)



(b)

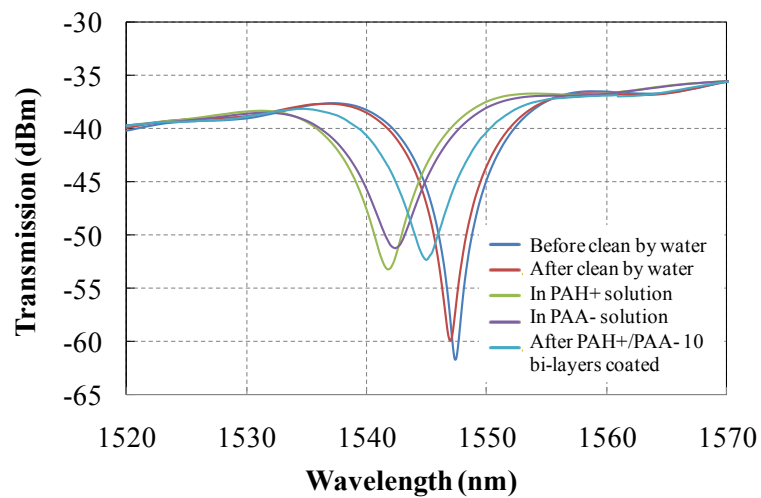
Figure 18. (a) Transmission spectra of SMF-28-LPG for various RH from 20% to 50% and (b) dependence of SMF-28-LPG resonance wavelength and transmission intensity on RH.

4.2 RH response of nanofilm-coated SMF-28-LPG

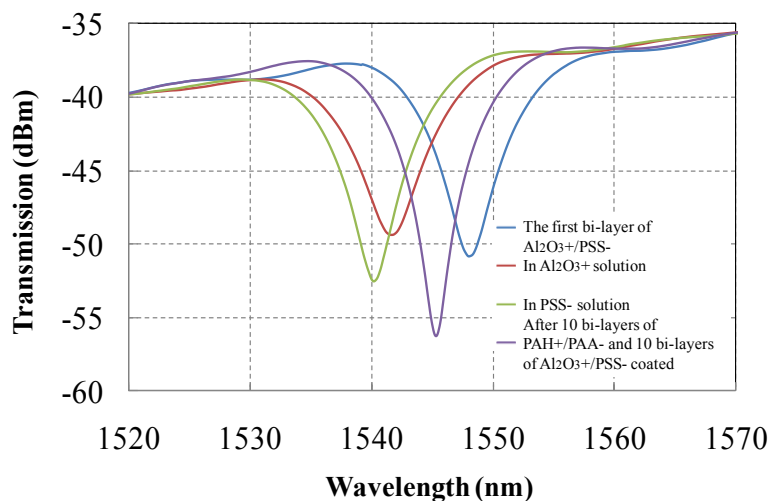
Sensitivity of a LPG to refractive index results from the dependence of the phase-matching condition on the effective refractive indices of the cladding modes that can be changed by the change of external refractive index. There are three cases which are that (1) external refractive index is lower than that of cladding; (2) external refractive index is equal to that of cladding; and (3) external refractive index is higher than that of cladding, all of which can influence the light to be coupled out of the core mode in a LPG. In the case of nanofilm-coated LPGs, the refractive index of the nanostructure material is larger than that of the cladding so that the resonance wavelength and coupling intensity are supposed to change after the nanofilms are deposited on the LPGs.

We have monitored the transmission spectra of SMF-28-LPG during the deposition process. Shown in Fig. 19(a) is the experimental evolution of the resonance spectral profiles of the grating coated with PAH+/PAA-. A slight shift of resonance wavelength was measured after the grating was cleaned by Milli-Q water. When the grating is immersed in PAH+ or PAA- solution, the shifts of resonance wavelength are -5.4 nm and 4.5 nm, respectively. After 10 bi-layers of PAH+/PAA- are deposited on the grating, the resonance wavelength is shifted from 1546.8 nm to 1544.6 nm, and the coupling intensity is reduced from -59.651 dBm to -51.889 dBm. Measured resonance wavelengths of SMF-28-LPG in polymer solutions and nanofilm-coated SMF-28-LPG are shorter than that of the grating after cleaning by Milli-Q water because the increase of external refractive index leads to an increase of effective refractive index

of coupled cladding mode and the resonance wavelength moves toward short wavelength, consistent with the phase-matching condition. Fig. 19(b) shows the experimental evolution of the grating transmission intensity deposited with Al_2O_3^+ /PSS- nanofilm on PAH+/PAA- nanofilm. At this stage, the resonance wavelength of the grating with 10 bi-layers of PAH+/PAA- nanofilm is located at 1546.3 nm with intensity of -51.203 dBm. The resonance wavelengths shift to 1541.6 nm and 1539.7 nm, respectively, when the PAH+/PAA- nanofilm-coated grating is put in Al_2O_3^+ and PSS- solutions. The resonance wavelength of the grating coated with those two nanofilms is at 1544.9 nm with increase of coupling strength at the transmission intensity of -55.696 dBm, which is due to the fact that the refractive index of Al_2O_3^+ /PSS- nanofilm is smaller than that of cladding and the transited cladding mode can be confined in the PAH+/PAA- nanofilm as it becomes a cylindrical waveguide. The final resonance wavelength shift is -1.9 nm from the grating cleaned to the grating coated with two nanofilms, which is not significant when compared with the whole wavelength region measured.



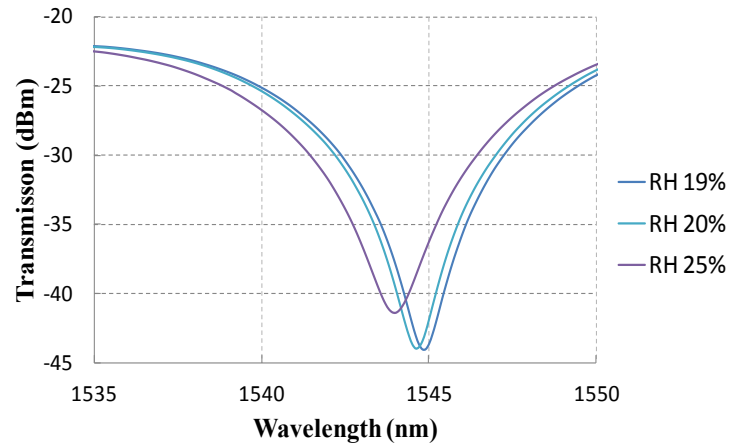
(a)



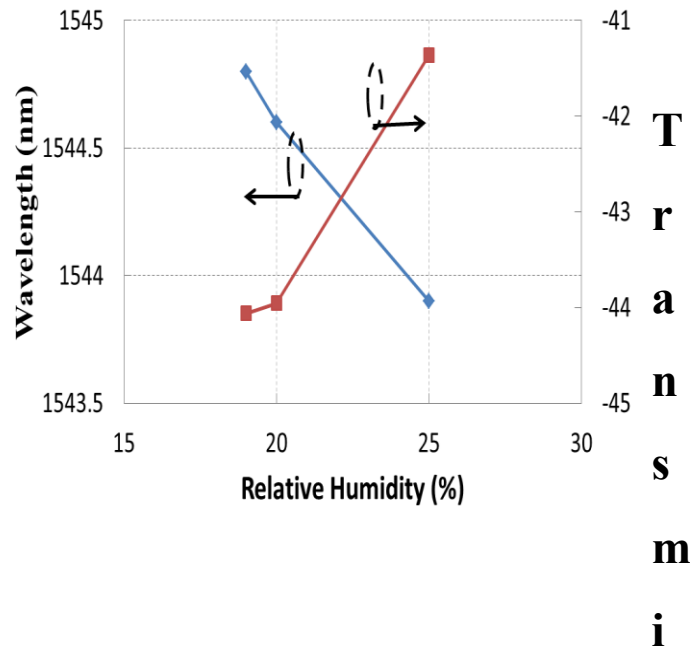
(b)

Figure 19. Experimental evolution of transmission spectra of SMF-28-LPG for: (a) the primary nanofilm before and after cleaned by Milli-Q water, in PAH^+ and PAA^- solutions, and after 10 bi-layers of $\text{PAH}^+/\text{PAA}^-$ coated and (b) the secondary nanofilm of the first bi-layer of $\text{Al}_2\text{O}_3^+/\text{PSS}^-$, in Al_2O_3^+ and PSS^- solutions, and after 10 bi-layer of $\text{Al}_2\text{O}_3^+/\text{PSS}^-$ coated.

Next, the responses of nanofilm-coated SMF-28-LPG to change of RH level were examined. Shown in Fig. 20(a) are the transmission spectra of this grating for different RH, and shown in Fig. 20(b) is the relationship of RH with resonance wavelength and transmission intensity. The total wavelength shift is -0.9 nm while total intensity change is -2.697dBm. The coefficients of nanofilm-coated SMF-28-LPG sensitivity to RH in terms of resonance wavelength shift and intensity change are about 0.00067%/pm and 0.0022%/10⁻³dBm, respectively. From the data processed above, we can see that there is more significant change in the resonance intensity than in the wavelength shift in humidity response of nanofilm-coated SMF-28-LPG.



(a)



(b)

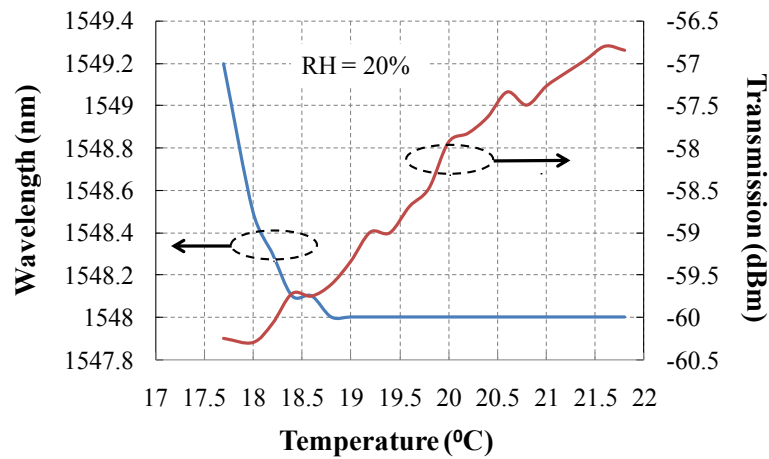
Figure 20. (a) Transmission spectra of nanofilm-coated SMF-28-LPG for various RH from 19% to 25% and (b) dependence of nanofilm-coated SMF-28-LPG resonance wavelength and transmission intensity on RH.

4.3 Temperature responses of SMF-28-LPG and nanofilm-coated SMF-28-LPG

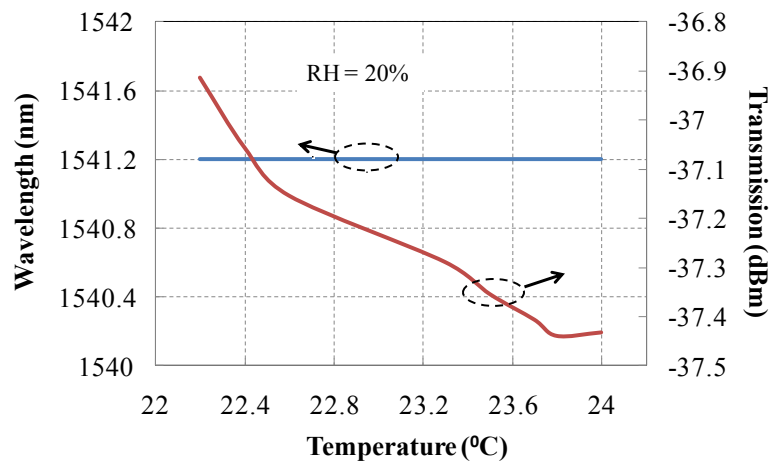
Temperature responses of SMF-28-LPG and nanofilm-coated SMF-28-LPG were tested at fixed RH of 20% corresponding to their resonance wavelength and transmission intensity for identifying cross-sensitivity and thermal stability. It is highly desired that the coupling resonance of the grating be temperature insensitive when it is used for humidity detection. It can be expected that the coefficient of PCF-LPG resonance wavelength shift to temperature should be low because the glass structure of the fiber is adjusted to the original state of the relaxation at silica transition temperature radiated by the CO₂ laser such that the grating is thermally stable under this temperature.

Fig. 21(a) and (b) show the temperature responses of SMF-28-LPG and nanofilm-coated SMF-28-LPG to resonance wavelength and transmission intensity at fixed RH of 20%. The dependence of temperature on resonance wavelength indicates that the blue shift of resonance wavelength in SMF-28-LPG is 1.2 nm from 17.7 °C to 18.8 °C while it becomes thermo stable from 18.8 °C to 21.8 °C, which shows that the grating inscribed by CO₂ laser is temperature insensitive above 18.8 °C at low RH. It is also observed that the resonance wavelength has no shift from 22.2 °C to 24 °C in nanofilm-coated SMF-28-LPG. It is interesting to note that the resonance intensity of SMF-28-LPG increases with increase of temperature, while it reduces when temperature increases in the case of nanofilm-coated SMF-28-LPG, from which it can be seen that the resonance coupling efficiency between core mode and cladding mode is a function of temperature. Moreover, as temperature goes up, water molecules trapped in the secondary

nanofilm can obtain more kinetic energy to get out of this film, leading to a smaller refractive index of the film and strengthening in the resonance coupling.



(a)

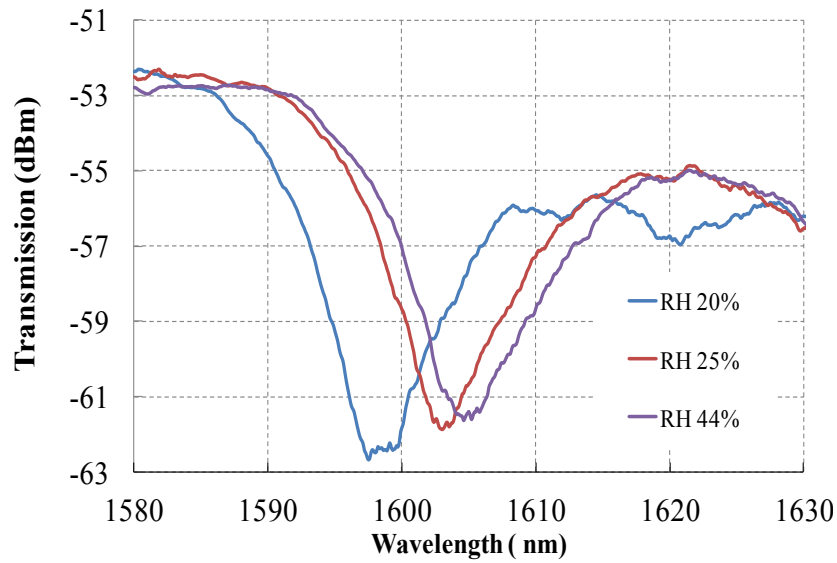


(b)

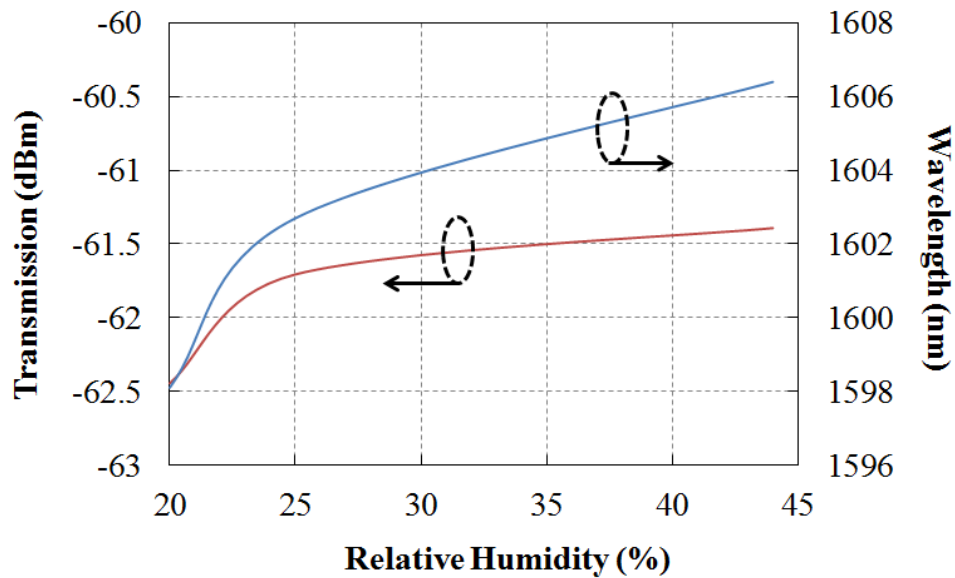
Figure 21. Temperature responses of resonance wavelength and transmission intensity at RH of 20% for: (a) SMF-28-LPG and (b) nanofilm-coated SMF-28-LPG.

4.4 RH response of exterior nanofilm-coated PCF-LPG

Both effective indices of core modes and cladding modes will change when the PCF-LPG experiences in a moisture environment, compared to the SMF-28-LPG where only the effective index of cladding changes. In Fig. 22(a) reveals that the slope of effective index change is larger in core than in cladding from RH of 20% to 44%, which leads the shift towards larger wavelength. Fig. 22(b) shows the dependence of nanofilm-coated PCF-LPG resonance wavelength and transmission intensity on different RH level. The coefficients of both average RH-wavelength and RH-intensity sensitivities are $0.0034\%/pm$ and $0.0269\%/10^{-3}dBm$, respectively.



(a)



(b)

Figure 22. (a) Transmission spectra of exterior nanofilm-coated PCF-LPG for RH spans from 20% to 44% and (b) dependences of exterior nanofilm-coated PCF-LPG resonance wavelength and transmission intensity on different levels of RH.

4.5 RH response of interior nanofilm-coated PCF-LPG

The experimental setup used for testing of interior nanofilm-coated PCF-LPG response to humidity is shown in Fig. 23. A broadband superluminescent light-emitting diode (SLED) light source is connected to a single-mode fiber that is clamped with a fiber clumper on a 3-D translation stage. The single-mode fiber is butt-connected to one end of the interior nanofilm-coated PCF-LPG, the other end of which is also butt-connected to another single-mode fiber that is clamped with a fiber clumper on a 3-D translation stage, and finally goes to an OSA. In this way, the moisture can be diffused through the air channels of the interior nanofilm-coated PCF-LPG. An optically aligned (within $+ 1\mu\text{m}$) single-mode fiber is used to couple light into and out of the interior nanofilm-coated PCF-LPG for signal collection. A home-made humidity chamber houses all of the 3-D translation stages, the interior nanofilm-coated PCF-LPG, a mini ultrasonic humidifier that consists of a digital temperature and the humidity meter.

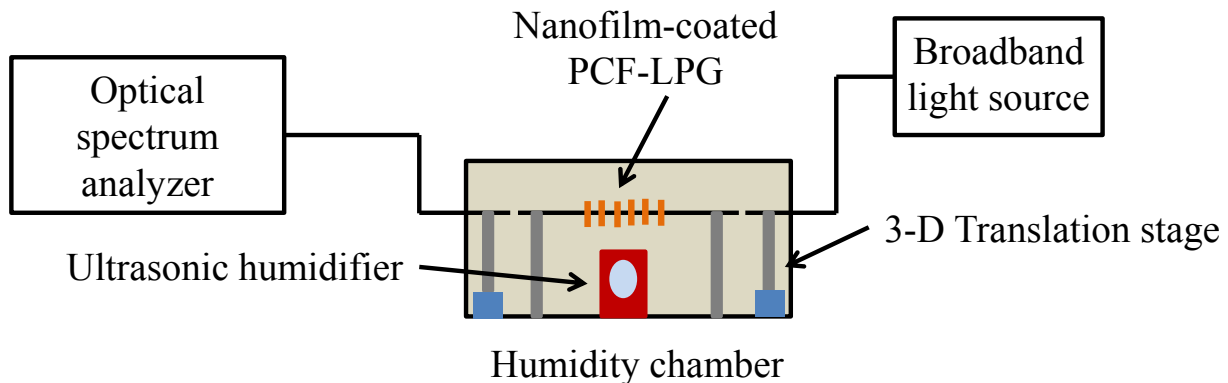
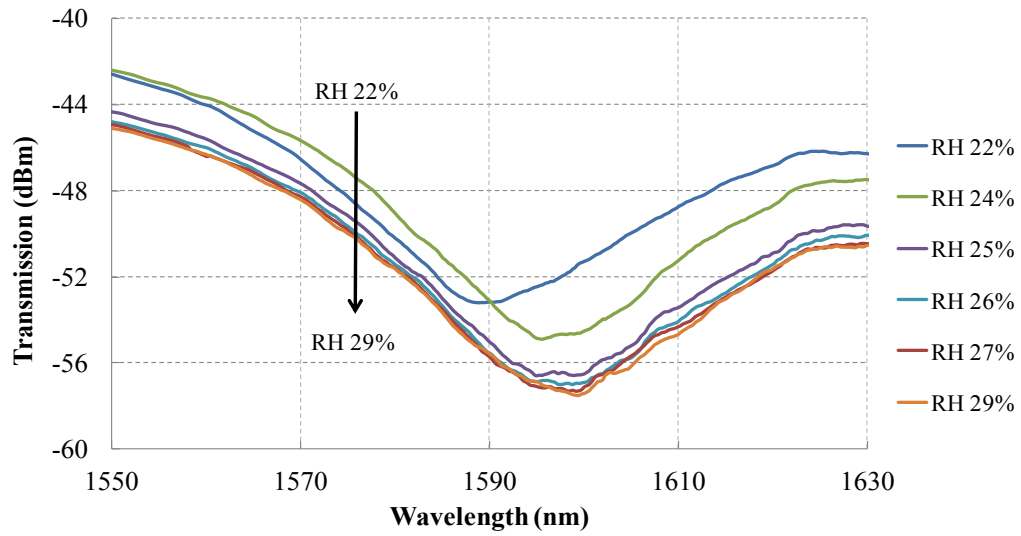


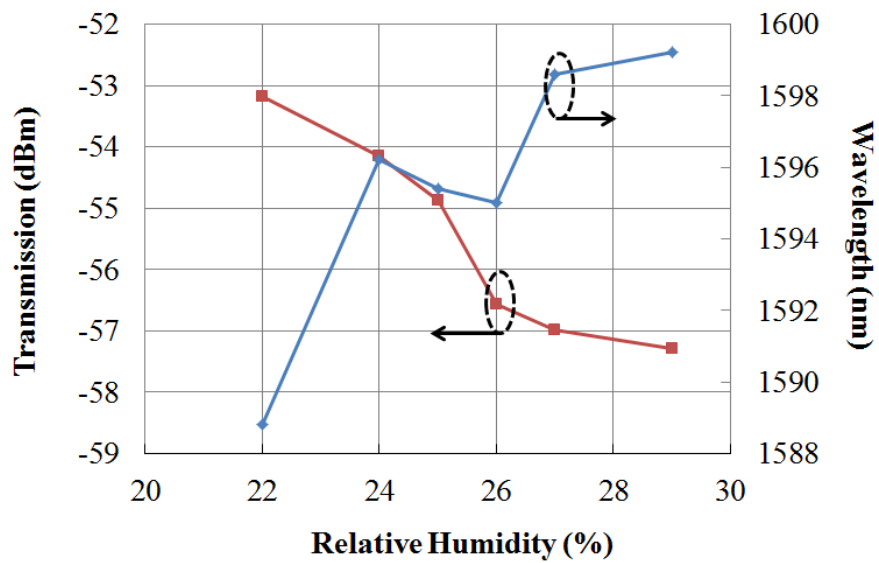
Figure 23. Experimental setup for Relative Humidity test by interior nanofilm-coated PCF-LPG

The responses of interior nanofilm-coated PCF-LPG to changing of RH at room temperature (24.5°C) have been tested. Shown in Fig. 24(a) are the transmission spectra of

interior nanofilm-coated PCF-LPG with different RH level, while Fig. 24(b) shows the dependences of resonance intensity and wavelength on RH. As the RH increase from 22% to 29%, more water molecules are adsorbed on the nanofilm, resulting in stronger light absorption from transited cladding mode. The transmission power of resonance dip gets significantly low, as indicated in Fig. 24(b). On the other hand, as indicated in the blue line in Fig. 24(b), when the secondary nano coating absorbs more water molecules while RH increasing, the effective refractive index of cladding increases and leads to a significant shift of resonance wavelength. Table 1 lists the average sensitivity comparison for different patterns of LPGs sensor for RH test. The average coefficient of RH-intensity is $0.0016\%/10^{-3}$ dBm and this level of sensitivity compares well to conventional LPG, nanofilm-coated LPG, and exterior nanofilm-coated PCF-LPG. The average coefficient of RH-wavelength is $0.0007\%/pm$ which is also more sensitive than other three types of LPGs



(a)



(b)

Figure 24. (a) Transmission spectra of interior nanofilm-coated PCF-LPG for RH spans from 22% to 29% and (b) dependences of interior nanofilm-coated PCF-LPG resonance wavelength and transmission intensity on different level of RH.

Table 2. Average RH Sensitivity Comparison for Different Sensors

	<i>RH-Wavelength Sensitivity*</i>	<i>RH-Intensity Sensitivity**</i>
<i>Conventional LPG</i>	RH 0.0136%/pm	RH 0.0519%/10 ⁻³ dBm
<i>Nano-Coated LPG</i>	RH 0.0067%/pm	RH 0.0022%/10 ⁻³ dBm
<i>Exterior Nanofilm-Coated PCF-LPG</i>	RH 0.0034%/pm	RH 0.0269%/10 ⁻³ dBm
<i>Interior Nanofilm-Coated PCF-LPG</i>	RH 0.0007%/pm	RH0.0016%/10 ⁻³ dBm
		RH 0.00022%/10 ⁻³ dBm ***

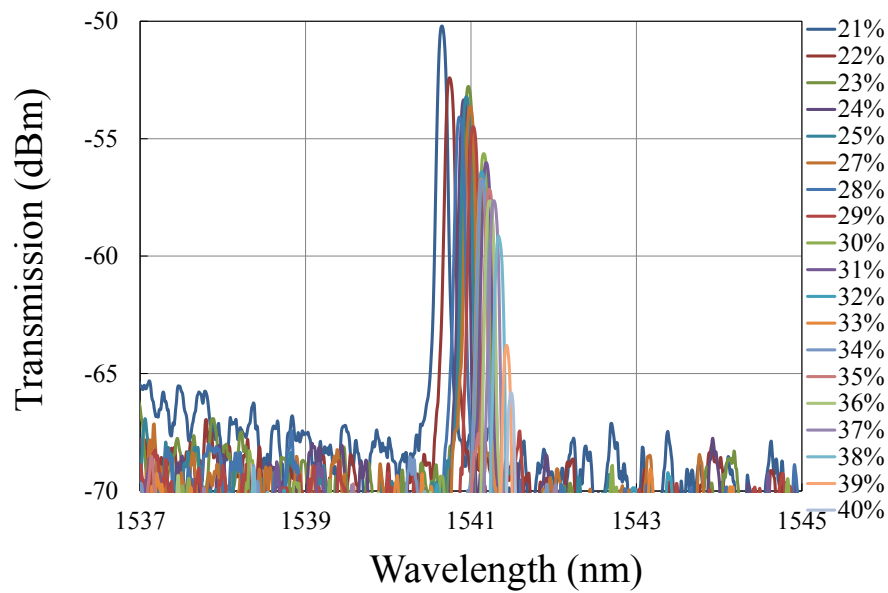
* Shift toward shorter wavelength is for conventional LPG and Nano-Coated LPG, and longer wavelength for PCF-LPG

** Transmission intensity of resonance is increased with increase of RH

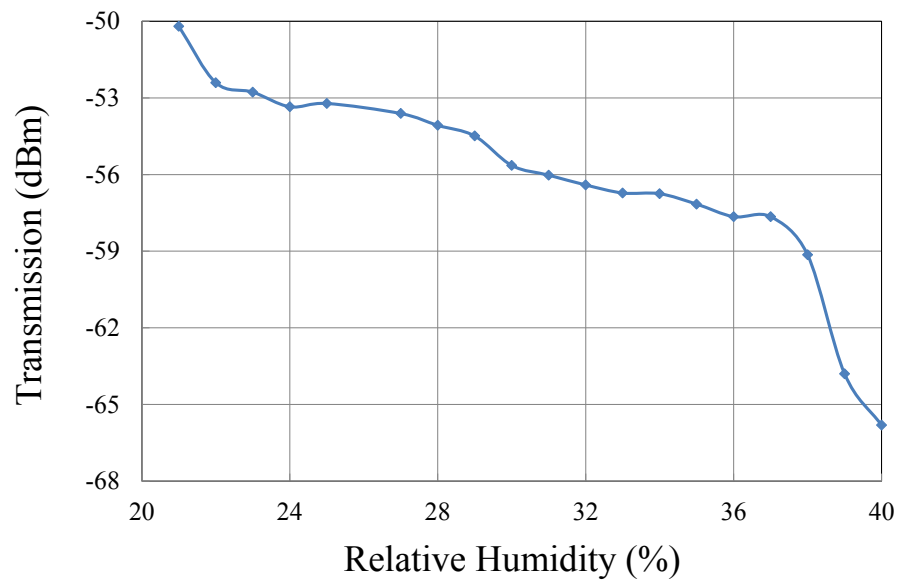
*** Highest sensitivity from HR 38% to 39% by using tunable Er-doped fiber ring laser as light source

Because the dependence of resonance intensity of interior nanofilm-coated PCF-LPG on RH is not a monotonic function, we used a tunable Er-doped fiber ring laser as the light source to tune the laser wavelength on the resonance wavelength of interior nanofilm-coated PCF-LPG obtaining the highest sensitivity for RH change of 1%. Fig. 25(a) shows the transmission spectra of interior nanofilm-coated PCF-LPG for RH spans from 21% to 40%, while Fig. 25(b) shows the dependences of interior nanofilm-coated PCF-LPG resonance transmission intensity. The highest sensitivity to resonance intensity change is at RH of 38%, which is 0.00022%/10⁻³dBm. The experimental results are listed in Table 1 for a comparison of average RH sensitivity with

different sensors



(a)



(b)

Figure 25. (a) Transmission spectra of interior nanofilm-coated PCF-LPG for RH spans from 21% to 40% and (b) dependences of interior nanofilm-coated PCF-LPG resonance transmission intensity on different level of RH by using a tunable Er-doped fiber ring laser as the light source.

Chapter 5--Tunable fiber ring laser absorption spectroscopic sensors for gas detection

With the rapid development of fiber-optic telecommunication technology, optical fibers are also quickly attractive for applications in sensing, controlling, and instrumentation [46-48]. A light source, some optical fibers, a sensing transducer, and a detector consist of an optical fiber sensing system. The basic operating principle of an optical fiber sensor is based on the fact that the transducer modulates the optical characteristics of the optical system, such as wavelength, intensity, phase, and polarization, which indicates a change in the properties of the optical signal received at the detector.

Optical fiber gas sensors [49, 50] have some inherent advantages over non-fiber types of gas sensing techniques, such as freedom from electromagnetic interference; high sensitivity and selectivity; immunity to combustion and explosion; and capability of sensing without temperature compensation. In addition, as its waveguide structure, optical fiber gas sensors provide a means of guiding laser radiation over long distance with minimum losses. The operating principle of optical fiber gas sensor is based on the absorption spectrum of gas analyte. Those absorbing wavelengths, like a characteristic fingerprint, result from vibrations and rotations of the gas molecules caused by the orbital transition of electrons in the visible and near-infrared (near-IR) spectral range that can be calculated with quantum mechanics. Because the light from optical fiber propagates through the gas sample with center wavelength close to the gas absorption line, the intensity of light is decreased and the gas analyte can be detected with the concentration that can be determined with the attenuation of light, which is abide by the

Beer-Lambert law that is expressed as:

$$I(\lambda)=I_0(\lambda)\exp(-\sigma l\rho) \quad (8)$$

where I and I_0 are, respectively, the light intensities at wavelength of λ with and without the presence of gas being detected; σ is the cross section of light absorption by a single gas molecule; l is the length of the fiber; and ρ is the gas density.

Tunable diode laser absorption spectroscopy (TDLAS) technologies to detect trace gases sensitively, selectively, and rapidly in situ in the near-IR spectral region have attracted for considerable research and development in recent years [51-54]. The advantage of TDLAS over other gas detection techniques for concentration measurement is its ability to achieve trace detection limits in the order of parts per billion (ppb). However, this technique has its drawbacks of bulk architecture and small change of signal on top of large background which decrease the signal-to-noise ratio (SNR) of the system. The large size of the gas detector can be overcome by using a tunable fiber ring laser instead of a tunable diode laser while two ways can be employed to improve the SNR; one is to reduce the noise in the signal, the other is to increase the absorption. We report, in this work, a tunable fiber ring laser absorption spectroscopic gas sensor which is based on a special fiber gas cell that is a segment of photonic crystal fiber (PCF) with a long-period grating (LPG) inscribed by CO₂ laser. The formation of a sensing head with gas cell facilitates that the laser light beam can be effectively coupled in to cladding of PCF at resonance wavelength by the LPG where the gas in air holes absorbs the light. The remaining light travels along the PCF cladding and is reflected at the end of the fiber where a silver mirror is coated at

the fiber facet. The distance between the LPG and silver mirror is about 10 mm so that the attenuation of the light is limited. The reflected light propagates back within cladding of LPG segment, passing through the gas cell one more time and thus increasing the sensing interaction length. The light is finally coupled back into the fiber core for intensity measurement that is inversely proportional to the concentration of gas (ammonia is used in our research work).

The remainder of this chapter is organized as follows: First, we present the design of the sensor head where core mode to cladding mode coupling and recoupling by a LPG in PCF is used with a specific aim of employing the cladding mode for absorption spectroscopic sensing, we then describe the fabrication of silver mirror on the fiber facet by e-beam evaporator coating technique. We then present the testing results of this fiber sensor by investigating the absorption band near wavelength of 1531 nm with NH_3 electron transitions. The chapter also includes a discussion on the relationship among the parameters of NH_3 concentration, intensity of tunable fiber laser, and absorption wavelength. In conclusion, we consider some potential applications of the fiber sensors in different fields and possible directions of future research and development in this area.

5.1 Design of Sensor Head

The fundamental principle of tunable fiber ring laser absorption spectroscopic sensors is based on the Beer-Lambert law which is given in Eq.(8). For a particular vapor, such as ammonia gas, the ratio of transmitted light intensities at wavelength of λ with and without the presence of

NH₃ is given by

$$I(\lambda)/I_0(\lambda) = \exp[-S_v(T) \cdot \phi_v \cdot P \cdot x_{\text{NH}_3} \cdot L] \quad (9)$$

Where $S_v(T)$ (cm⁻²·atm⁻¹) is the temperature-dependent absorption line strength for a specific transition of v ; ϕ_v (cm) is the line-sharp function with a normalization feature as that $\int_0^\infty \phi_v(v) dv \equiv 1$; x_{NH_3} is the mole fraction of ammonia gas; P (atm) that is the total pressure; and L is the optical path length.

The absorption line strength as a function of temperature can be given by [12]

$$S_v(T) = S_v(T_0) \frac{Q(T_0)}{Q(T)} \left(\frac{T_0}{T}\right) \exp\left[-\frac{h \cdot c \cdot E_v''}{k} \left(\frac{1}{T} - \frac{1}{T_0}\right)\right] \times \left[1 - \exp\left(\frac{-h \cdot c \cdot v_{0,v}}{kT}\right)\right] \times \left[1 - \exp\left(-\frac{h \cdot c \cdot v_{0,v}}{kT_0}\right)\right]^{-1}$$

where $Q(T)$ is the ammonia's partition function, and $v_{0,v}$ and E_v'' are the frequency and the lower-state energy of the transitions, respectively. The total ammonia internal partition function $Q(T)$ can be expressed by

$$Q(T) = Q_{\text{nuclear}}(T) \times Q_{\text{rotational}}(T) \times Q_{\text{vibrational}}(T) \quad (11)$$

where $Q_{\text{nuclear}}(T)$, $Q_{\text{rotational}}(T)$, and $Q_{\text{vibrational}}(T)$ are the nuclear, rotational, and vibrational partition functions, respectively.

Table 3 shows the two absorption lines (I and II at 22.85 °C) of ammonia molecule that we used in our experiments. Absorption line I is an isolated transition of ammonia whereas absorption line II is the overtone transition of NH₃. The line strength is to be expected to increase up to 4% at temperature between 26.85 °C and 39.85 °C so that line I and II can be useful for the

measurement of ammonia concentration.

Table 3. Ammonia absorption lines.

Wavelength ^⓪ (nm) ^⓪	Line	Line strength at 296 K (cm ⁻² ·atm ⁻¹)	Frequency (cm ⁻¹)
1548.68 ^⓪	I	0.057784	6528.76
6528.89	II 1548.65 ^⓪		0.0307

To build a highly integrated optical absorption fiber sensing system for practical applications, it is desirable to fabricate the silver or gold mirror on the facet of an optical fiber for light reflection. Shown in Fig. 26 is a schematic diagram of core mode to cladding mode coupling and recoupling in a PCF-LPG with a silver coating as a mirror at the facet of the fiber. The tunable laser beam, the intensity distribution and the profile of which are respectively shown in the left image at bottom of Fig. 26 and Fig. 26(a), is first injected into the PCF core; then light in the core is coupled to a cladding mode at the resonance wavelength of LPG. The coupled cladding mode travels along the cladding and the power distribution and profile of this cladding mode are shown in the right image at the bottom of Fig. 26.

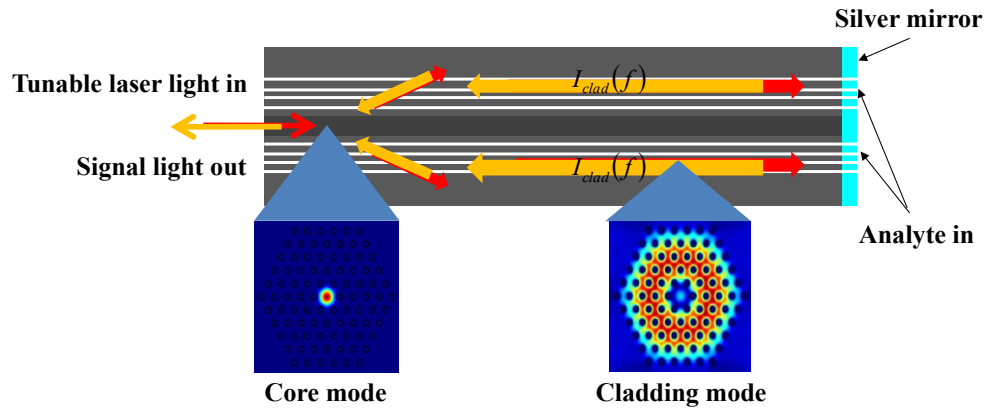


Figure 26. Schematic diagram of core mode to cladding mode coupling and recoupling in a PCF-LPG with a silver mirror at the facet of the fiber. The left and right images in the bottom figure are the simulated power distributions of core mode and cladding mode, respectively.

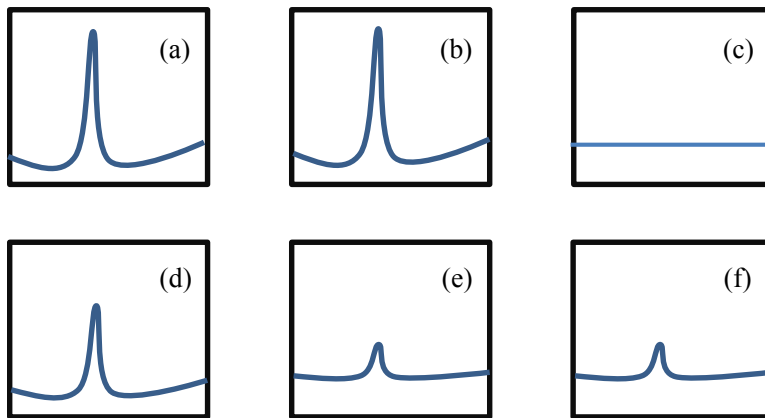


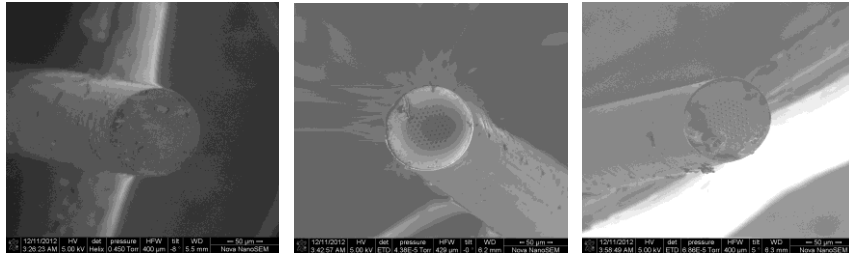
Figure 27. Expected spectra of core mode and cladding mode coupling and recoupling in the sensor head with a silver mirror at fiber facet: (a) tunable laser incident in PCF; (b) after LPG in PCF cladding; (c) after LPG in PCF core; (d) before reflection in PCF cladding; (e) before recoupling from PCF cladding at LPG; and (f) signal light out of PCF core, respectively.

When light propagates to the end of the fiber which is ~ 10 mm from the grating with a small attenuation in the cladding, it reflects back by a silver mirror that is coated on the fiber facet. The evanescent field of light is absorbed by gas species in the air channels of the cladding before reflection and the expected profile of light is shown in Fig. 27(d). The reflected light travels along the cladding of the LPG segment again and passes through the gas species one more time, thus increasing the absorption length. Shown in Fig. 27(e) is the light profile before recoupling into core from cladding at the LPG. The light is finally coupled to core for its intensity measurement and the signal light profile from core is shown in Fig. 27(f). The PCF-LPG sensing head can easily be constructed in the following way: inscription of one LPG in PCF by CO₂ laser and deposition of silver film by e-beam evaporator coating technique on one end of the fiber which is close to LPG.

5.2 Fabrication of sensor head

The fiber in which we used to inscribe LPGs is the solid core single-mode PCF (type-D) with the following parameters of optical and geometrical properties: attenuation at 1550 nm of 4.9 dB/km; core, air-channel, and fiber cladding diameters of 9.2 μm , 3.1 μm , and 126 μm , respectively; and air-channel distance of 126 μm . For the measurements and comparison of reflectivity with silver coating on fiber facet, we have also used the SMS-28 normal optical fiber and the solid core single-mode PCF (type-B) with parameters: attenuation at 1550 nm of 1.5 dB/km; core, air-channel, and fiber cladding diameters of 8.5 μm , 2.9 μm , and 6 μm ,

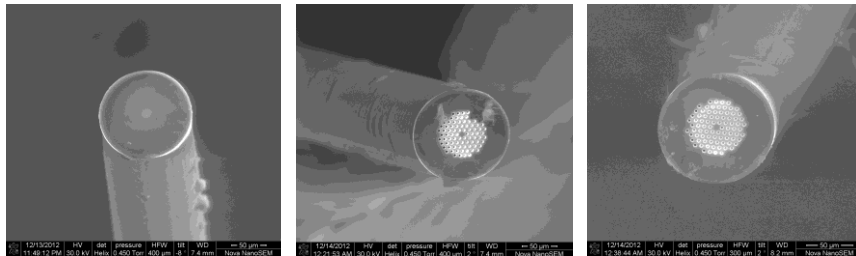
respectively; and air-channel distance of $6.4 \mu\text{m}$.



(a)

(b)

(c)



(d)

(e)

(f)

Figure 28. SEM images of fiber facets coated with silver coatings: (a) normal fiber, (b) PCF type-B, (c) PCF type-D, and cleaved fiber cross-sections from 10 mm of silver coated fiber facets: (d) normal fiber, (e) PCF-type-B, (f) PCF type-D.

Three types of fibers including SMF-28, PCF type-B, and PCF type-D, have been deposited with silver on their one end-facet using e-beam evaporator coating technique. The fibers are first cleaved at one end, and then are loaded on sample plate in the e-beam evaporator (AUTO 500 Edwards). In order to deposit silver on fiber facet uniformly, the fibers need to be rotated during the deposition. The coating thickness can be monitored by setting up the thickness monitor. The evaporation rate is 0.2 nm/s. The thickness of silver coating is about 50 nm. Fig. 28(a), (b), and (c) present SEM images of normal fiber facet, PCF type-B facet, and PCF type-D facet, which are deposited with silver coatings, respectively, while Fig. 28(d), (e), and (f) show respective SEM images of cleaved fiber cross-sections of normal fiber, PCF type-B, and PCF type-D, which are from 10 mm of silver coated facets. We can see, from those SEM images, that there is no silver ion diffusion into air channels in cladding during deposition process.

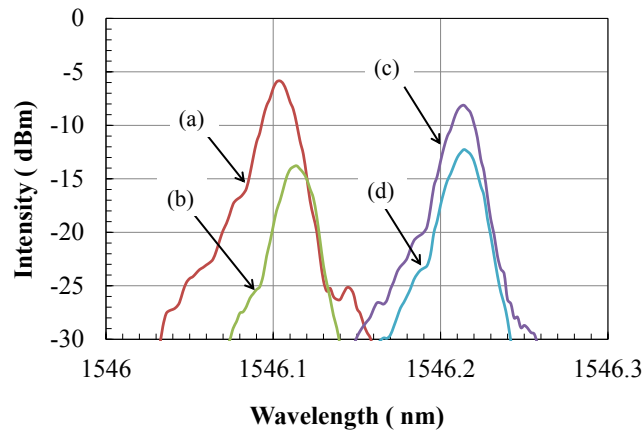


Figure 29. Optical spectra: (a) output of diode laser at wavelength around 1546 nm, (b) reflection intensity of normal fiber with silver mirror at fiber facet, (c) reflection intensity of PCF type-B with silver mirror at fiber facet, and (d) reflection intensity of PCF type-D with silver mirror at fiber facet.

The reflectivities of fibers with silver coating as an optical mirror on their facets have been measured with normal optical fiber, PCF type-B, and PCF type-D, the experimental setup of which can be described as follows: the light power at wavelength around 1546 nm from a laser diode is directed into the 20% arm of 20:80 1 x 2 optical fiber coupler at wavelength of 1550 nm, then the light is coupled to the other end of the coupler where the fiber coated with silver on its facet is connected, finally the reflected light goes back to the coupler and an OSA is used to measure the reflectivity of the fiber at the 80% arm of the coupler. Fig. 29(a) shows the optical spectrum of diode laser output, and Fig. 29(b), (c), and (d) shows the reflected optical spectra of normal optical fiber, PCF type-B, and PCF type-D with silver mirror on the fiber facet, respectively. Listed in Table 4 are reflection parameters of those three types of fibers, of which the reflectivities are 20.09%, 73.91%, and 28.51, respectively. Different refractivity is attributed to the factors that are coating thickness, roughness of fiber facet, and coating uniformity as well as splicing losses between PCFs and FC/APC connectors. We will use the highest reflectivity of PCF-LPG in the experiments for gas detection.

Table 4. Reflection parameters of normal fiber, PCF type-B, and PCF type-D with silver mirrors on the fiber facets.

Reflectivity [Ⓢ] (mW)	Thickness of mirror (50 nm) (%) [Ⓢ]	Incident intensity (mW)	80% incident intensity	Reflected intensity (mW)
	0.042	Normal fiber 20.09 [Ⓢ]	0.2604	
0.154	PCF type-B 73.91 [Ⓢ]	0.2604		0.2083
0.059	PCF type-D 28.51 [Ⓢ]	0.2604		0.2083

5.3 Tunable Er-doped fiber ring laser

Due to the fact that the absorption lines of ammonia transitions are located at wavelength around 1531 nm, we perform the absorption spectroscopic sensing of ammonia gas by employing a low noise Er-doped fiber ring laser that can be continuously turned over 40 nm in the C-band and measuring the absorption spectrum of ammonia transition with a PCF-LPG gas cell of sensor head.

Shown in Fig. 30 is a schematic layout of the tunable Er-doped fiber ring laser with a fiber Fabry-Perot tunable filter (FFP-TF) and a fiber Sagnac loop. A 7-m long Er-doped fiber is pumped with a 160 mW continuous wave (CW) diode laser at wavelength of 980 nm through a wavelength-division multiplexing (WDM) 980 nm/1550 nm fiber coupler that mixes signal with pump power. As the pump light propagates along the Er-doped fiber, it inverts the population of erbium ions and results in the generation of forward and backward propagating amplified spontaneous emission (ASE) in the C-band.

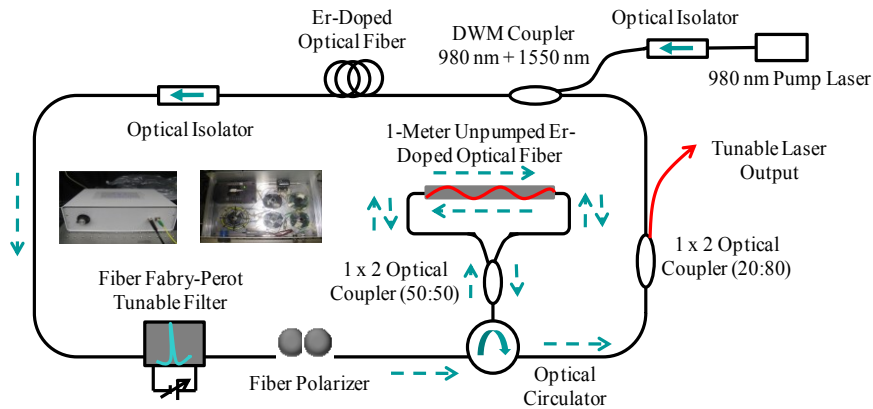


Figure 30. Schematic diagram of tunable Er-doped fiber ring laser with the FFP-TF and the Sagnac loop.

The insets show the tunable ring laser device box (left) and the interior components of the tunable ring laser (right) absorption. One optical isolator is placed at the output of the Er-doped fiber to ensure the unidirectional lasing operation and prevent any feedback that could cause instabilities in the tunable Er-doped fiber laser cavity. A FFP-TF provides a first-stage wavelength selection. A fiber polarizer is installed in the tunable Er-doped fiber ring laser cavity to suppress the competition between polarization modes in the fiber ring. By using a 50% - 50% fiber coupler and 3-port optical fiber circulator, a Sagnac loop is introduced with an unpumped 1-m long Er-doped fiber. Through local gain saturation of the unpumped Er-doped fiber caused by the interference standing wave and resultant spatial hole burning, the all-fiber long intensity pattern leads to a periodic modulation of the fiber gain, This gain modulation behaves as a Bragg grating that

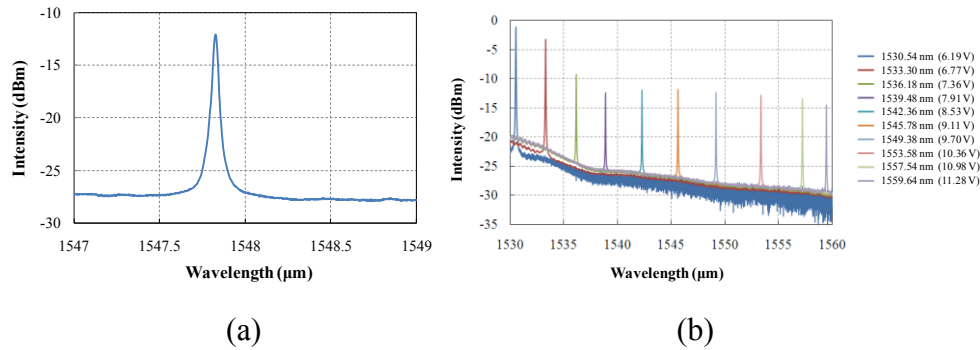


Figure 31. (a) Optical output power spectrum of tunable Er-doped fiber ring laser, and (b) the entire optical output power spectra of tunable laser with wavelength turning range from 1530.54 nm to 1559.64 nm acts as a spectral filter with an estimated full-width at half-maximum (FWHM) of about 75 pm, corresponding to frequency of ~ 100 MHz.

The two-wave mixing fiber filter efficiently suppresses the multiple longitudinal modes created in the laser cavity, thus allowing for the creation of a single longitudinal mode laser source with lower noise level. The optical output from the tunable Er-doped fiber ring laser is obtained by tapping off a portion of light directed to a photo-detector and an OSA using an 80% - 20% fiber coupler. The total length of the ring cavity is about 16 m, resulting in a longitudinal mode spacing of 9.7 MHz. All fiber components are fusion spliced to reduce back-reflection and increase transmission between the components. The tunable Er-doped fiber ring laser is packaged in an aluminum box with dimensions of 35 cm \times 25 cm \times 10 cm, which is shown in the left inset of Fig. 31. Shown in the right inset of Fig. 31 are the optical components of the laser inside the box.

5.4 Experimental setup

Schematic diagram of sensing measurement setup is depicted in Fig. 32. It consists of a 980 nm diode pump laser, two optical isolators at 980 nm and 1550 nm, respectively, a 980 nm/1550 nm WDM coupler, an Er-doped fiber around 25 m, a 3-port optical circulator, a pigtailed FFP-TF, a polarization controller, a 80%-20% 1 x 2 optical coupler, and a sensing head (gas cell) whose effective length is about 12 cm. One end of the sensing probe is connected to the optical circulator with FC/APC connector, which enables the sensing head with more favorable performance such as longer working distance and lower insertion losses. In this setup, one end of sensing head is used as both an analyte inlet for direct “sniffing” and a port for reentry of the transmitted light upon reflection from silver mirror at the fiber facet. The attenuation of the signal induced by the gas is proportional to the gas concentration and to be determined by the system which includes an OSA for absorption intensity measurement. The performance of the gas sensor is closely influenced by the output signal power, tuning range, and sensitivity which are determined by a number of critical parameters: ring-cavity loss, length of Er-doped fiber, output coupler ratio. With the use of a compact tunable ring laser, this arrangement can be made portable for field evaluation.

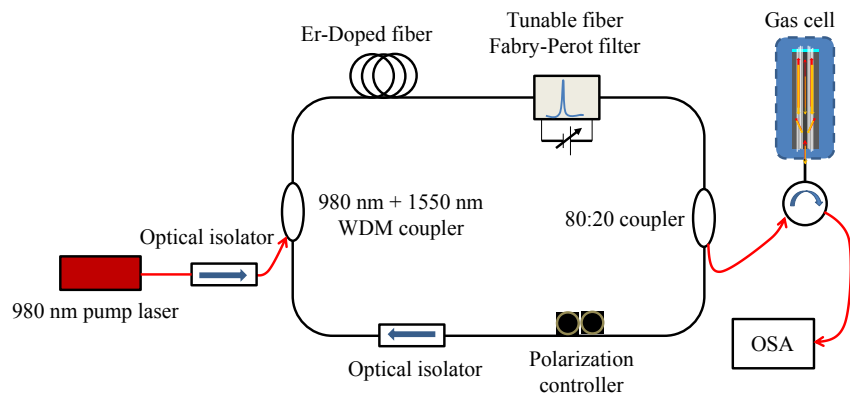


Figure 32. Experimental setup for the absorption spectroscopic ammonia gas sensing.

An important achievement through the measurements is that the sensing capacity relies upon the spectroscopic approach that is a rather general detection method applicable to a broad variety of gases and is in addition highly selective due to the specific vibrational-rotational states (fingerprint) for every gas. Er-doped fiber is used as the gain medium in the tunable fiber ring laser because its broad gain bandwidth covers absorption lines of gases of interest and permits multi-gas detection without changing light source. Specifications of sensing device, such as sensitivity, resolution, and response time for gas diffusion, can be optimized by appropriate fiber design, the cladding mode selected for recoupling process, mode coupling mechanism by external perturbation, and characteristics of the tunable fiber ring laser.

5.5 Testing results

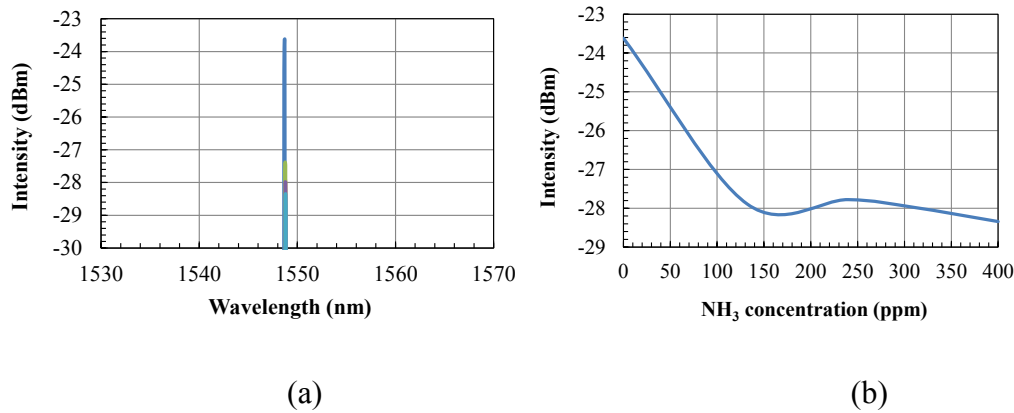


Figure 33. (a) Optical spectrum of diode laser at wavelength of 1548.4 nm and (b) dependence of absorption laser intensity on ammonia concentration.

Two types of laser sources, diode laser and tunable fiber ring laser, have been used in the measurements of absorption intensity. Shown in Fig. 33(a) is an optical spectrum of diode laser that is employed for detection of ammonia via overtone transition of NH₃ at wavelength around 1548.4 nm by absorption of laser intensity. Several different concentrations of NH₃ have been tested. The reflected light from PCF-LPG sensor head is about -23.618 dBm (~ 4.347 μ W), and measured intensity is about -28.255 dBm (~ 1.494 μ W) when NH₃ concentration reaches 165 ppm from 0 ppm in the gas chamber. The rate of power absorption is 65.7% while absorption sensitivity is about 17.3 nW/ppm at linear range of concentration. Shown in Fig. 33(b) is the relationship between absorption intensity and NH₃ concentration. It can be clearly seen that the

absorption intensity decreases linearly with increase of NH_3 concentration in the range between 0 and 165 ppm. The NH_3 molecules are saturated and condensates on the surface of air channels in PCF cladding, after its concentration is larger than 165 ppm so that the resultant sensing head possesses high sensitivity at low NH_3 concentration.

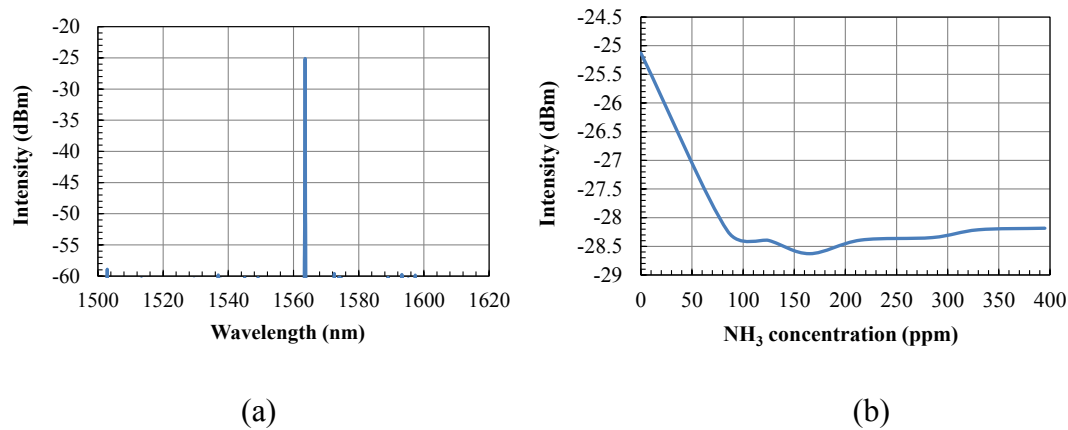


Figure 34. (a) Optical spectrum of tunable fiber ring laser at wavelength of 1563.6 nm and (b) dependence of absorption laser intensity on ammonia concentration.

The measurement of ammonia has been also conducted with tunable fiber ring laser. Shown in Fig. 34(a) is an optical spectrum of tunable Er-doped fiber ring laser at wavelength of 1563.6 nm which is one of six harmonic and combination bands at wavelength of near-IR range and selected for monitoring of NH_3 . The reflected intensity from sensor head without ammonia absorption is about -25.127 dBm (~ 3.071 μW). As NH_3 concentration goes up, the absorption intensity goes down. The absorption intensity of -28.238 dBm (~ 1.5 μW) correspond to

ammonia concentration of 125 ppm, below which the absorption intensity also decreases linearly. In this case, the absorption rate is about 51.2% and the sensitivity is 12.6 nW/ppm which is slightly less than that in the diode laser case. Shown in 34(b) is the dependence of absorption laser intensity on ammonia concentration. The trend of relationship between absorption intensity and NH_3 concentration is almost the same in both diode laser source and tunable fiber ring laser source, but tunable fiber ring laser source has its broad gain bandwidth that covers absorption lines of different gases of interest and permits multi-gas detection without changing the light source.

5.6 Conclusion

We designed and fabricated a sensing head that is a segment of PCF induced with a LPG on it and can be integrated with a tunable Er-doped fiber ring laser for an absorption spectroscopic sensor for gas detection. The wavelength of the fiber ring laser can be continuously tuned in C-band so that the absorption spectra of transition lines of different gases can be obtained with a high SNR without changing laser sources during the operation of detection. The experiment to measure the concentration of NH_3 gas has been conducted and the results reveal that this gas sensor system could realize high sensitivity and selectivity for gas tracing.

REFERENCES

- [1] Corrosion Costs and Preventive Strategies in the United States, NACE International, 2002
- [2] George F. Hays, "Now is the time", The World Corrosion Organization
- [3] M. P. Delisa, Z. Zhang, M. Shiloach, S. Pilevar, C. C. Davis, J. S. Sirks, W. E. Bentley, Evanescent wave long-period fiber Bragg grating as an immobilized antibody biosensor, *Anal. Chem.* 72 (2000) 2895-2900.
- [4] T. Venugopalan, T. Sun, K. T. V. Grattan, Long-period grating-based humidity sensor for potential structural health monitoring, *Sens. Actuators A* 148 (2008) 57-62.
- [5] B.D. Gupta, , D.K. Sharma, "Evanescent wave absorption based fiber optic pH sensor prepared by dye doped sol-gel immobilization technique." *Optics Communications*, Volume 140, 32-35, 1997
- [6] J. Bürck, J. -P. Conzen, H. -J. Ache," A fiber optic evanescent field absorption sensor for monitoring organic contaminants in water," *Fresenius' Journal of Analytical Chemistry*, 342:394-400, (1992)
- [7] Cordeiro, C. M. B., Franco, M. A. R., Chesini, G., Barretto, E. C. S., Lwin, R., Cruz, C. H. B., and Large, M. C. J., "Microstructured-core optical fiber for evanescent sensing applications," *Opt. Express* 14(26), 13056-13066 (2006).
- [8] Yu, X., Sun, Y., Ren, G. B., Shum, P., Ngo, N. Q., and Kowk, Y. C., "Evanescent field absorption sensor using a pure-silica defected-core photonic crystal fiber," *IEEE Photo. Technol. Lett.* 20(5), 336-338 (2008).

- [9] Frazão, O., Santos, J. L., Araújo, F. M., and Ferreira, L. A., "Optical sensing with photonic crystal fibers," *Laser & Photon. Rev.* 2(6), 449-459 (2008).
- [10] Polynkin, P., Polynkin, A., Peyghambarian, N., and Mansuripur, M., "Evanescent field-based optical fiber sensing device for measuring the refractive index of liquids in microfluidic channels," *Opt. Lett.* 30(11), 1273-1275 (2005).
- [11] Zhu, Y., He, Z., Kaňka, J., and Du, H., "Numerical analysis of refractive index sensitivity of long-period gratings in photonic crystal fiber," *Sens. Actuators B* 129, 99-105 (2008).
- [12] Knight, J. C., "Photonic crystal fibers," *Nature* 424(6950), 847-851 (2003).
- [13] Russell, P. St. J., "Photonic crystal fibers," *Science* 299(5605), 358-362 (2003).
- [14] Birks, T. A., Knight, J. C., and Russell, P. St. J., "Endlessly single-mode photonic crystal fiber," *Opt. Lett.* 22(13), 961-963 (1997).
- [15] Limpert, J., Schreiber, T., Nolte, S., Zellmer, H., Tunnerman, A., Liew, R., Lederer, F., Broeng, J., Vienne, G., Petersson, A., and Jakobsen, C., "High-power air-clad large-mode-area photonic crystal fiber laser," *Opt. Express* 11(7), 818-823 (2003).
- [16] Dudley, J. M., Genty, G., and Coen, S., "Supercontinuum generation in photonic crystal fiber," *Rev. Mod. Phys.* 78(4), 1135-1184 (2006).
- [17] Varshey, S. K., Saitoh, K., and Koshiba, M., "A novel design for dispersion compensating photonic crystal fiber Raman amplifier," *IEEE Photo. Technol. Lett.* 17(10), 2062-2064 (2005).

- [18] Sazio, P. J. A., Amezcua-Correa, A., Finlayson, C. E., Hayers, J. R., Scheidemantal, T. J., Baril, N. F., Jackson, B. R., Won, D.-J., Zhang, F., Margine, E. R., Gopalan, V., Crespi, V. H., and Badding, J. V., "Microstructured optical fibers as high-pressure microfluidic reactors," *Science* 311(5767), 1583-1589 (2006).
- [19] Couny, F., Benabid, F., and Light, P. S., "Subwatt threshold cw Raman fiber-gas laser based on H₂-filled hollow-core photonic crystal fiber," *Phys. Rev. Lett.* 99(14), 143903 (2007).
- [20] Vengsarkar, A. M., Pedrazzani, J. R., Judkins, J. B., Lemaire, P. J., Bergano, N. S., and Davidson, R., "long-period fiber-grating-based gain equalizers," *Opt. Lett.* 21(5), 336-338 (1996).
- [21] Erdogan, T., "Cladding-mode resonances in short- and long-period fiber grating filters," *J. Opt. Soc. Am. A* 14(8), 1760-1773 (1997).
- [22] Yariv, A., "Coupled-mode theory for guided-wave optics," *IEEE J. Quantum Electron.* 9(9), 919-933 (1973).
- [23] Hill, K. O., Fujii, Y., Johnson, D. C., and Kawasaki, B. S., "Photosensitivity in optical fiber waveguides: Application to reflection filter fabrication," *Appl. Phys. Lett.* 32(10), 647-649 (1978).
- [24] Mohammed, M. and Gu, X., "Long-period grating and its application in laser beam shaping in the 1.0 μm wavelength region," *Appl. Opt.* 48(12), 2249-2254 (2009).
- [25] Shin, W., Lee, Y. L., Yu, B.-A., Noh, Y.-C., and Oh, K., "Spectral characterization of helicoidal long-period fiber gratings in photonic crystal fibers," *Opt. Comm.* 282(12), 3456-3459

(2009).

[26] Patrick, H. J., Kersey, A. D., Bucholtz, F., "Analysis of the response of long period fiber gratings to external index of refraction," J. Lightwave Technol. 16(9), 1606-1612 (1998).

[27] Rindorf, L., Jensen, J. B., Bufva, M., Pedersen, L. H., Høiby, and Bang, O., "Photonic crystal fiber long-period gratings for biochemical sensing," Opt. Express 14(18), 8224-8231 (2006).

[28] Dobb, H., Kalli, K., and Webb, D. J., "Measured sensitivity of arc-induced long-period grating sensors in photonic crystal fiber," Opt. Comm. 260(1), 184-191 (2006).

[29] He, Z., Zhu, Y., and Du, H., "Effect of macro-bending on resonant wavelength and intensity of long-period gratings in photonic crystal fiber," Opt. Express 15(4), 1804-1810 (2007).

[30] Polynkin, P., Polynkin, A., Peyghambarian, N., and Mansuripur, M., "Evanescent field-based optical fiber sensing device for measuring the refractive index of liquids in microfluidic channels," Opt. Lett. 30(11), 1273-1275 (2005).

[31] G. Decher, J.D. Hong and J. Schmitt, "Buildup of ultrathin multilayer films by a self-assembly process: III. Consecutively alternating adsorption of anionic and cationic polyelectrolytes on charged surfaces," Thin Solid Films 210/211, 831 (1992).

[32] Yariv, A., "Coupled-mode theory for guided-wave optics," IEEE J. Quantum Electron. 9(9), 919-933 (1973).

[33] Rindorf et al, "Photonic crystal fiber long-period grating for biochemical sensing,"

Optics Express, vol. 14, no. 18, pp. 8224-8231, 2006

[34] J. M. Corre, I. R. Matias, I. D. Villar, F. J. Arregui, Design of pH sensors in long-period fiber gratings using polymeric nanocoatings, IEEE Sens. J. 7 (2007) 455-463.

[35] I. D. Villar, M. Achaerandio, I. R. Matias, F. J. Arregui, Deposition of overlays by electrostatic self-assembly in long-period fiber gratings, Opt. Lett. 30 (2005) 720-722.

[36] I. D. Villar, I. R. Matias, F. J. Arregui, Enhancement of sensitivity in long-period fiber gratings with deposition of low refractive-index materials, Opt. Lett. 30 (2005) 2363-2365.

[37] A. Cusano, A. Iadicicco, P. Pilla, L. Contessa, S. Campopiano, A. Cutolo, Cladding mode reorganization in high-refractive-index-coated long-period gratings: effects on the refractive-index sensitivity, Opt. Lett. 30 (2005) 2536-2538.

[38] I. D. Villar, I. Matias, F. Arregui, P. Lalanne, Optimization of sensitivity in long period fiber gratings with overlay deposition, Opt. Express 13 (2005) 56-69.

[39] Z. Wang, J. R. Heflin, R. H. Stolen, S. Ramachandran, Highly sensitive optical response of optical fiber long-period gratings to nanometer-thick ionic self-assembled multilayers, Appl. Phys. Lett. 86 (2005) 223104.

[40] A. Cusano, P. Pilla, L. Contessa, A. Ladicicco, S. Campopiano, A. Cutolo, High-sensitivity optical chemosensor based on coated long-period gratings for sub-ppm chemical detection in water, Appl. Phys. Lett. 87 (2005) 234105.

[41] A. Cusano, P. Pilla, L. Contessa, S. Campopiano, A. Cutolo, M. Giordano, G. Guerra, Coated long-period gratings as high-sensitivity optochemical sensors, J. Lightwave Technol. 24

(2006) 1776-1786.

- [42] J. M. Corres, I. D. Villar, I. R. Matias, F. J. Arregui, Two-layer nanocoatings in long-period fiber gratings for improved sensitivity of humidity sensors, *IEEE Trans. Nanotechnol.* 7 (2008) 394-400.
- [43] A. Cusano, A. Iadicicco, P. Pilla, L. Contessa, S. Campopiano, A. Cutolo, Mode transition in high refractive index coated long period grating, *Opt. Express* 14 (2006) 19-34.
- [44] Zheng, S., Zhu, Y., and Krishnaswamy, S., "Nanofilm-coated long-period fiber grating humidity sensors for corrosion detection in structural health monitoring," *Proc. SPIE* 7983, 79831A-8 (2011).
- [45] J. Pfizner, Poiseuille and his law, *Anaesthesia* 31 (1976) 273-275.
- [46] Giallorenzi, T. G., Bucaro, J. A., Dandridge, A., Sigel, Jr., G. H., Cole, J. H., and Rashleigh, S. C., "Optical fiber sensor technology," *IEEE J. Quantum Electron.*, QE-18(4), 626-665 (1982).
- [47] O'Farrell, M., Lewis, E., Flanagan, C., Lyons, W. B., and Jackman, N., "Design of a system that uses optical-fiber sensors and neural networks to control a large-scale industrial oven by monitoring the food quality online," *IEEE Sensors J.* 5(6), 1407-1420 (2005).
- [48] Claus, R. O., Kapp, D. A., and Murphy, K. A., "Fiber-optic sensors using high-resolution optical time domain instrumentation systems," *J. Lightwave Technol.* 8(9), 1273-1277 (1990).
- [49] MacCraith, B. D., McDonagh, C. M., O'Keefe, G., Keyes, E. T., Vos, J. G., O'Kelly, B.,

- and McGlip, J. F., "Fiber optic oxygen sensor based on fluorescence quenching of evanescent-wave excited ruthenium complexes in sol-gel derived porous coatings," *Analyst* 118(4), 385-388 (1993).
- [50] Francisco, J. A., Matias, I. R., and Claus, R. O., "Optical fiber gas sensors based on hydrophobic alumina thin films formed by the electrostatic self-assembly monolayer process," *IEEE Sensors J.* 3(1), 56-61, (2003).
- [51] Martin, P. A., "Near-infrared diode laser spectroscopy in chemical process and environmental air monitoring," *Chem. Soc. Rev.* 31(6), 201-210 (2002).
- [52] Werle, P., Mücke, R., D'Amato, F., and Lancia, T., "Near-infrared trace-gas sensors based on room-temperature diode lasers," *Appl. Phys. B* 67(5), 307-315 (1998).
- [53] Weidmann, D., Kosterev, A. A., and Tittel, F. K., "Application of a widely electrically tunable diode laser to chemical gas sensing with quartz-enhanced photoacoustic spectroscopy," *Opt. Lett.* 29(16) 1837-1839 (2004)
- [54] Zhou, X., Liu, X., Jeffries, J. B., and Hanson, R. K., "Development of a sensor for temperature and water concentration in combustion gases using a single tunable diode laser," *Meas. Sci. Technol.* 14(7), 1459-1468 (2003).